

34496



National Library of Canada

Bibliothèque nationale du Canada

CANADIAN THESES ON MICROFICHE

THÈSES CANADIENNES SUR MICROFICHE

NAME OF AUTHOR / NOM DE L'AUTEUR LARRY SYDORA

TITLE OF THESIS / TITRE DE LA THÈSE EFFECTS OF THE HOLOGRAM  
ON THE LITHOSPHERE

UNIVERSITY / UNIVERSITÉ ALBERTA

DEGREE FOR WHICH THESIS WAS PRESENTED /  
GRADE POUR LEQUEL CETTE THÈSE FUT PRÉSENTÉE Master of Science

YEAR THIS DEGREE CONFERRED / ANNÉE D'OBTENTION DE CE GRADE Fall 1977

NAME OF SUPERVISOR / NOM DU DIRECTEUR DE THÈSE Edo Ryland

Permission is hereby granted to the NATIONAL LIBRARY OF CANADA to microfilm this thesis and to lend or sell copies of the film.

L'autorisation est, par la présente, accordée à la BIBLIOTHÈQUE NATIONALE DU CANADA de microfilmer cette thèse et de prêter ou de vendre des exemplaires du film.

The author reserves other publication rights, and neither the thesis nor extensive extracts from it may be printed or otherwise reproduced without the author's written permission.

L'auteur se réserve les autres droits de publication; ni la thèse ni de longs extraits de celle-ci ne doivent être imprimés ou autrement reproduits sans l'autorisation écrite de l'auteur.

DATED / DATÉ August 24/77 SIGNED / SIGNÉ Larry Sydora

PERMANENT ADDRESS / RÉSIDENCE FIXE 187  
Innisfree, Alberta,  
Canada, T0B 2G0



National Library of Canada

Cataloguing Branch  
Canadian Theses Division

Ottawa, Canada  
K1A 0N4

Bibliothèque nationale du Canada

Direction du catalogage  
Division des thèses canadiennes

## NOTICE

The quality of this microfiche is heavily dependent upon the quality of the original thesis submitted for microfilming. Every effort has been made to ensure the highest quality of reproduction possible.

If pages are missing, contact the university which granted the degree.

Some pages may have indistinct print especially if the original pages were typed with a poor typewriter ribbon or if the university sent us a poor photocopy.

Previously copyrighted materials (journal articles, published tests, etc.) are not filmed.

Reproduction in full or in part of this film is governed by the Canadian Copyright Act, R.S.C. 1970, c. C-30. Please read the authorization forms which accompany this thesis.

**THIS DISSERTATION  
HAS BEEN MICROFILMED  
EXACTLY AS RECEIVED**

## AVIS

La qualité de cette microfiche dépend grandement de la qualité de l'original soumis au microfilmage. Nous avons tout fait pour assurer une qualité supérieure de reproduction.

S'il manque des pages, veuillez communiquer avec l'université qui a conféré le grade.

La qualité d'impression de certaines pages peut laisser à désirer, surtout si les pages originales ont été dactylographiées à l'aide d'un ruban usé ou si l'université nous a fait parvenir une photocopie de mauvaise qualité.

Les documents qui font déjà l'objet d'un droit d'auteur (articles de revue, examens publiés, etc.) ne sont pas microfilmés.

La reproduction, même partielle, de ce microfilm est soumise à la Loi canadienne sur le droit d'auteur, SFC 1970, c. C-30. Veuillez prendre connaissance des formules d'autorisation qui accompagnent cette thèse.

**LA THÈSE A ÉTÉ  
MICROFILMÉE TELLE QUE  
NOUS L'AVONS REÇUE**

THE UNIVERSITY OF ALBERTA

RELEASE FORM

NAME OF AUTHOR: LARRY J. SYDORA

TITLE OF THESIS: EFFECTS OF THE DOWNGOING  
LITHOSPHERE

DEGREE FOR WHICH THESIS WAS PRESENTED: MASTER OF SCIENCE

YEAR THIS DEGREE GRANTED: 1977

Permission is hereby granted to the UNIVERSITY OF ALBERTA LIBRARY to reproduce single copies of this thesis and to lend or sell such copies for private, scholarly or scientific research purposes only.

The author reserves other publication rights, and neither the thesis nor extensive extracts from it may be printed or otherwise reproduced without the author's written permission.

(SIGNED) .....

*Larry J. Sydora*

PERMANENT ADDRESS:

..Box 187.....

..Innisfree, Alberta.....

..Canada...T0R 2G0.....

DATED August 9th... 1977

THE UNIVERSITY OF ALBERTA

EFFECTS OF THE DOWNGOING

L. C. W. HERE

BY

LARRY J. SYDORA



A THESIS

SUBMITTED TO THE FACULTY OF GRADUATE STUDIES AND RESEARCH

IN PARTIAL FULFILMENT OF THE REQUIREMENTS FOR THE DEGREE

OF MASTER OF SCIENCE

IN GEOPHYSICS

DEPARTMENT OF PHYSICS

EDMONTON, ALBERTA

FALL, 1977

THE UNIVERSITY OF ALBERTA  
FACULTY OF GRADUATE STUDIES AND RESEARCH

The undersigned certify that they have read, and recommend to the Faculty of Graduate Studies and Research, for acceptance, a thesis entitled EFFECTS OF THE DOWNGOING LITHOSPHERE submitted by LARRY J. SYDORA in partial fulfilment of the requirements for the degree of Master of Science in Geophysics

*[Handwritten Signature]*  
.....  
Supervisor  
*[Handwritten Signature]*  
.....  
.....  
.....

Date ... August 9th ... 1977

## ABSTRACT

The local temperature field of a downgoing slab is investigated by using a finite-difference numerical approach. A numerical model which simulates the downgoing slab is used to study the effects of various dip angles, different rates of subduction, heat sources and rising material from the upper surface of the slab. The model assumes a simple descent mechanism near the surface and this mechanism is discussed in terms of the associated earthquake field and the interactions of the material there. The rate of subduction and amount of shear-strain heating along the upper surface of the slab are important factors in the determination of the thermal regime. When melting occurs, rising material from the top of the slab produces high heat flow values at the surface of the earth on the continental side of the oceanic trench. The gravity effects of the downgoing lithosphere are also investigated. The results indicate that the presence of rising melt will mask the gravity effect of the cold sinking slab at low subduction velocities (i.e. 1 cm/year).

The behaviour of time-varying electromagnetic fields corresponding to various temperature distributions associated with a subducting lithospheric slab has been studied using a two-dimensional numerical model. The results show that the movement of melted material from the top of the slab considerably affects the spatial behaviour of the electromagnetic field components at the surface,

particularly that of  $H_z$  and  $H_z/H_y$ . A lateral conductivity contrast at the surface (i.e. a sea-land interface) completely dominates the behaviour of the field components there, and the effect of any subsurface temperature variations is negligible.

## Acknowledgements

This work would not have been accomplished without the encouragement and advice I received from my supervisor, Dr. P.W. Jones, for which I am grateful.

I would like to thank E. E. Nyland and Dr. R. St. J. Lambert for their helpful suggestions and revisions.

I wish to express my gratitude to Dr. V. Ramaswamy who provided the computer programs necessary for the electromagnetic modelling and with whom I worked closely.

I was fortunate in being able to discuss various aspects of gravity effects related to lithospheric motion with Dr. D. Dyrelus and wish to express my thanks for the subroutine he provided for the gravity computations.

Thanks are due to the following individuals for their encouragement and helpful suggestions: H.T.S. Enders, F.C. Salevsky, G. Churney, J. Lee, and Dr. S. Cahay.

Financial support was obtained from a grant to Dr. P.W. Jones from the National Research Council of Canada. I am grateful for the teaching assistantship awarded to me during the 1976-1977 term by the Department of Physics. I wish to express my appreciation to Chevron Standard Ltd. for their graduate scholarship.



## TABLE OF CONTENTS

CHAPTER	PAGE
1. INTRODUCTION .....	1
2. THE NUMERICAL MODEL .....	11
2.1 Lithospheric Slab Translation .....	11
2.2 Temperature Field Computation .....	15
2.3 The Initial and Boundary Conditions .....	16
2.4 Heat Sources .....	19
2.5 Rising Melt .....	21
2.6 Gravity Calculations .....	22
3. THERMAL REGIMES FOR DOWNGOING SLABS .....	25
3.1 Comparison of the Diagonal Translation Method and the Linear and Toksoz Method .....	25
3.2 Thermal Regimes for Slabs with Different Dip Angles .....	30
3.2.1 Dip Angle of $26.6^\circ$ .....	30
3.2.2 Dip Angle with Changes with Depth .....	34
3.3 Thermal Regimes for Slabs with Heat Sources ...	35
3.3.1 Subduction Rate of 0.7 cm/year .....	38
3.3.2 Subduction Rate of 5.6 cm/year .....	48
3.4 Gravity Effects of the Downgoing Slab .....	55
3.5 Summary of Results .....	61
4. THE EFFECT OF SUBSURFACE TEMPERATURE VARIATIONS ON THE BEHAVIOUR OF TIME-VARYING ELECTROMAGNETIC FIELDS .....	65
4.1 Description of the Models .....	65
4.2 Discussion of Results .....	71
4.3 Summary of Results .....	80
REFERENCES .....	82

LIST OF TABLES

Table	Description	Page
1.	Geometry of Active Volcanoes in Indonesia, Lesser Antilles and New Zealand .....	47

LIST OF FIGURES

FIGURE	Page
1. Schematic representation of the transition procedure .....	17
2. The variation of density with depth .....	18
3. Comparison of the diagonal translation procedure with the circular arc procedure .....	26
4. As Fig. 3, but at 21.26 million years .....	27
5. As Fig. 3, but at 35.44 million years .....	28
6. The temperature regime and surface heat flow for a subducting slab with dip angle $26.6^\circ$ at 10.63 million years after the start of subduction .....	31
7. As Fig. 6, but at 21.26 million years .....	32
8. As Fig. 6, but at 35.44 million years .....	33
9. A downgoing slab with dip angles $26.6^\circ$ and $45.0^\circ$ ..	36
10. A downgoing slab with dip angles $26.6^\circ$ and $56.3^\circ$ ..	37
11. The temperature regime and surface heat flow profile for a descending slab with a dip angle of $45^\circ$ at 70.88 million years after the start of subduction .....	39
12. Temperature profiles along the upper surface of the slab for the models of Fig. 11 (curve A) and Fig. 10 (curve B) .....	40
13. As Fig. 11, but with a dip angle of $26.6^\circ$ and a slab velocity of 1.6 cm/year .....	41
14. The temperature regime and surface heat flow profile for a $45^\circ$ dipping slab with rising melt ...	45
15. As Fig. 14, but with a dip angle of $26.6^\circ$ .....	46
16. The temperature regime and surface heat flow profile for a $45^\circ$ dipping slab with a velocity of 8.0 cm/year .....	49
17. As Fig. 16, but with adiabatic compression and shear heating included as heat sources .....	51
18. Temperature-depth profiles along the upper surface	

of the slab for Fig. 17 (curve 1) and for a slab dipping at $45^\circ$ with the same heat source as in Fig. 17 .....	67
19. As Fig. 18, but with shear heating increased by 15% .....	68
20. Gravity profiles across the horizontal extent of subduction for a $45^\circ$ dipping slab .....	68
21. Gravity profiles across the horizontal extent of subduction for a $26.8^\circ$ dipping slab .....	69
22. Temperature distribution and electrical conductivity models for (a) initial state, and (b) final state .....	70
23. The geophysical model .....	70
24. The spatial variation of heat flow and the electromagnetic field components at the surface $z=0$ for different conductivity models .....	71
25. Contours of equal amplitude of temperature and electromagnetic fields for different conductivity models .....	77
26. The spatial variation of $H_x/H_y$ and $E_x$ at the surface $z=0$ for different upper layer conductivity contrasts .....	78

2. Debate over the location of the ridge axis and the movement of lithospheric plates in the downwelling and back-arc region, and the region of the subduction zone. Reduction in the amount of volcanic activity and the amount of the total atmospheric gas flux (e.g., Bishop et al., 1973; Leonard et al., 1974). In recent years, little has been developed in the investigation of the chemical composition of the atmosphere, particularly in the island arc regions associated with them (expansion of the site, 1968; Res. Rep. no. 10, 1968; 1969; 1970; 1971; and others). Such investigations seek to develop a model of the descending atmosphere which is consistent with various geophysical and geologic data available.

One of the most important geophysical observations that in recent years has been surface heat flow in relation to subduction zones. One of the first heat flow maps constructed on a world scale was that compiled by Lee and Uyeda (1965). It included heat flow measurements from ocean trench and island arc regions. The ocean trenches were found to have heat flow values averaging  $0.99 \pm 0.61$  H.F.U. (H.F.U. = microcalories/cm<sup>2</sup>-sec), substantially lower than the surface mean heat flow of  $1.5 \pm 10\%$  H.F.U. Island arc regions had widely scattered heat flow values with a mean of  $1.36 \pm 0.54$  s.d. (standard deviation), H.F.U., although a large

number of the measurements were above the surface mean heat flow. A more up-to-date heat flow map (Von Herzen and Lee, 1969) indicated abnormally high heat flow values associated with island arc regions. Horai and Uyeda (1969) found anomalously high heat flow values associated with volcanic areas that were related to island arcs. Most heat flow observations taken to date have been found in the Sea of Japan where heat flow values average  $2.01 \pm 0.38$  s.d., H.F.U. (Sugimura and Uyeda, 1973). Since island arc regions in general are associated with volcanic areas, it is generally believed that most other island arcs display a corresponding high heat flow pattern.

In the past several years many studies have investigated possible causes of anomalous heat flow values related to subduction zones as well as thermal regimes associated with the descent of the earth's lithosphere in these regions. Oxburgh and Turcotte (1968) determined that frictional heating may play an important role in generating high heat flow in island arc regions. According to their analytical calculations, production of magmas occurs between 100 km and 200 km depth, where temperatures are high enough on the descending lithosphere's fault zone to produce significant partial melt. The partial melt was hypothesized to rise to the earth's surface creating an anomalous heat flow region. McKenzie and Sclater (1968) investigated high heat flow in the northwest Pacific and determined that possible sources of heat included volcanic

intrusion into the crust and dissipative shear heating in the mantle due to the descending lithosphere's motion. Calculations demonstrated that shear heating near the earth's surface or an increase in thermal conductivity due to mass transport of magma could explain the high heat flow, although the initial temperatures needed were unrealistic.

McKenzie (1969) obtained a temperature distribution in the lithosphere thrust beneath an island arc region. Flow and stress heating in the mantle maintained a high heat flow anomaly in the island arc. The analysis assumed the temperature gradient below the lithosphere followed the adiabatic gradient and the descending lithosphere acted as a thermal boundary layer supporting temperature and density gradients larger than those in the surrounding mantle. The heat flow anomaly in the 'real world' situation could then be explained if there existed a large shallow stress field to produce shearing near the earth's surface. The calculations included a large number of linearized approximations.

Oxburgh and Turcotte (1970) assumed frictional dissipation of heat occurred along the fault zone near the upper surface of the descending slab and established a line heat source along this zone with source strength as a function of depth. They found that most of the heat was transferred to the descending lithosphere and the heat source was unable to generate enough heat to correspond to high heat flow in the island arc region. Minear and Tokoz

(1970) and Toksoz et al (1971) used a finite-difference solution of the conservation of thermal energy equation to determine the effects of spreading rate, adiabatic compression, radioactivity, phase changes and strain heating on the thermal regime of the downgoing lithospheric slab. They were unable to generate the heating required to produce a heat flow anomaly in the island arc region. Hasebe et al (1970) considered two-dimensional time dependent heat conduction equations with large heat generation along the deep-earthquake fault zone and effective heat transfer due to rising magma in the upper mantle above this zone. It was determined that heat generation four times as high as the mean heat flow at the upper surface of the lithosphere and heat conduction ten times as high as normal phonon conduction were required to explain anomalously high heat flow in the island arc region. The values used were justified by invoking viscous heat generation due to shear stress and penetrative convection of magma.

Griggs (1972) established a thermal model of the descending lithosphere which included gravity effects and possible earthquake mechanisms related to slab motion. Richter (1973) proposed fluid dynamic models of the lithosphere-asthenosphere system which included generalized mantle convection. He obtained flow patterns within the mantle for idealized models assuming the mantle acted as a Newtonian fluid. Turcotte and Schubert (1973) determined temperatures around the descending lithosphere using



constant shear stress on the fault zone as well as stress weakly dependent upon depth. The analytic model assumed partial melting occurred along the fault zone below the point where active volcanoes lie. The temperatures and shear stresses agreed with the models proposed by Toksoz et al (1971).

Andrews and Sleep (1974) used numerical modelling of flow induced by the downgoing slab to explain high heat flow in marginal basins and island arc volcanism. The induced flow was two-dimensional, time-dependent and included viscosity dependent upon temperature and pressure. The highest stress occurred at the base of the slab interface creating a narrow channel for separating melt from source materials, obtaining volcanic magma. In marginal basins tensile yielding caused the plate to thin and raise heat flow values. Bird et al (1975) computed thermal regimes for continent-continent convergence zones modelled by the finite-difference technique of Toksoz et al (1971). Their model of the Zagros mountain region satisfied gravity, seismic, heat flow and geologic constraints.

Spence (1977) established a slabbing, escalator-like descent mechanism for the subducting Pacific plate. He proposed that partial melt is concentrated in a thin tabular zone of mantle above the plate. Partial melt is concentrated by episodic pressure reductions due to viscoelastic rebound induced by loading of the mantle. Partial melting caused by deeper pressure pulses rises to the underthrust plate.

creating a marginal basin.

The above studies indicate that there is interest in the interaction between the descending slab material and the surrounding medium as well as the form of the downwarping mechanism near the surface, though very little has been published on this latter point. In the work of Minear and Toksoz (1970) as well as Toksoz et al (1971) the thermal regime of a  $45^\circ$  dipping slab was investigated. It also appears that in most discussions concerning theoretical calculations for downgoing slabs, a  $45^\circ$  dip angle has been assumed. It is known that the earthquake zones (fault zones), which are taken to define the upper boundary of the downgoing slab, dip at various angles depending upon depth and the region being considered, not necessarily at  $45^\circ$  (see Sykes, 1966; Benioff, 1954). The dip angles may vary from approximately  $15^\circ$  in the Zagros mountain region and  $22^\circ$  for the near surface portion of the slab near the west coast of South America to as much as  $75^\circ$  in the deeper Bonin-Honshu region. In this regard Bird et al (1975) have recently considered slabs with shallower slopes ( $30^\circ$  and  $15^\circ$ ) and, as has been mentioned, have applied their method to the Zagros mountain region.

It is also apparent from the profiles of earthquake epicenters that the dip angle of many zones changes from a smaller angle near the surface to a greater angle at depth or that zones may flatten out at greater depth. If we identify these zones of earthquake activity with the upper

boundary of the slab, the implication is that the moving lithospheric plate must 'bend' at depth as well as initially near the earth's surface.

Several conductivity structures which are postulated to account for various regional geomagnetic field anomalies are attributed to variations in the temperature below the earth's surface (Uyeda and Rikitake, 1970; Law and Riddihough, 1971; Gough, 1973, Garland, 1975). Variations in the subsurface temperature may be either due to large-scale tectonic activity in the crust and mantle regions or they may be associated with the subduction of lithospheric plates into the upper mantle. Examples of geomagnetic anomalies that are attributed to tectonic activity include those observed at Alert (Rikitake and Whitham, 1964; Niblett et al, 1969), Northern Germany (Schmucker, 1959, Knodel, 1968) and Texas (Schmucker, 1964). Rikitake and Whitham (1964) suggested that certain features of the Alert anomaly could be explained by the rise of the 1400-1500° isotherms to within 25 km of the earth's surface. Schmucker (1964) attributed the Texas conductivity anomaly to the rise of the high temperature isotherms in the upper mantle. This interpretation by Schmucker has been supported to a large extent by the heat flow observations of Warren et al (1969). Comparing their heat flow observations with the geomagnetic observations of Schmucker (1964), Warren et al (1969) found that regions where Schmucker observed large anomalies in the horizontal magnetic component and small anomalies in the

vertical magnetic component, had high heat flow near the ground surface.

Two well known examples of geomagnetic anomalies observed in subduction zones are the Japanese anomaly and the Andean anomaly of Peru. It has been suggested (Gough, 1973, Garland, 1975) that both of these anomalies are related not only to the downward movement of the cold plate, but also the upward movement of hot material produced by the frictional heating along the surface of the descending lithosphere.

Although an exact relationship between geomagnetic field anomalies and heat flow anomalies is yet to be developed, it is believed that the anomalies observed in the horizontal magnetic components are more closely correlated with heat flow variations than anomalies in the vertical magnetic component (Rikitake, 1966). Large values in the horizontal components are generally associated with an increased heat flow.

Recent studies indicate that the descending slab remains cooler than the surrounding mantle to depths of 600 km to 700 km. The slab experiences shear-strain heating as it descends along the upper surface, although the amount of strain heating and its effect remain an area of controversy. A less certain quantity is the amount of heating produced by conduction to the interior of the slab as it descends. This is a key factor for the mechanism of slab

descent indicates that the slab experiences normal faulting as it begins to subduct followed by thrust faulting implying the slab acts as a distinct mechanically separate unit from the surrounding mantle. The effect that density and temperature variations have on the associated gravity and electromagnetic fields above descending slabs is still uncertain. Current studies also indicate that the descending slab does not maintain a constant dip angle as it descends.

Considering these aspects of the evidence of slab motion, it is of interest to develop a model which can provide for a range of dip angles as well as for the general case of a change in dip angle at depth. This gives a flexible model which may be used to determine variations in geophysical parameters at depth and near the earth's surface. It is then possible to investigate the lower limiting case of conditions required to produce melting on the upper surface of the downgoing slab. Several theoretical models for the thermal evolution of a downgoing slab are considered, including varying dip angle, inclusion of various heat sources at depth, and rising material from the top of the slab. This allows for the development of a model which predicts the possible loci of melting at depth and variations of heat flow at the surface.

The properties of the earth's interior can be better understood if data can be collected by various geophysical methods (i.e. heat flow, gravity, seismic, and magnetotelluric measurements) and correlated with each

other. In recent years, studies involving such detailed correlation are becoming more common (Garland, 1975). Nevertheless, geophysical surveys involving the simultaneous use of more than one method may not always be practicable.

One relatively simple means of undertaking a correlation study between various methods is through use of computer modelling. A numerical model is established to compare the thermal properties of a descending slab and the associated gravity effects. A comparison is also undertaken to determine the relationship between heat flow anomalies and electromagnetic field anomalies for a two-dimensional model as well as the electromagnetic effects of temperature variations within the descending slab. Electrical conductivity models are derived from temperature distributions for various thermal models.

## CHAPTER 2 THE NUMERICAL MODEL

In the numerical model to be presented, the dynamics of lithosphere motion are assumed and perturbations in various geophysical quantities are calculated on the basis of the dynamics. This numerical method is based on that originally developed by Minear and Toksoz (1970). The region of interest is divided into a two-dimensional grid with initial conditions specified at each grid point. Computation of the temperature field proceeds by using the thermal energy balance equation and the Peaceman and Rachford alternating-direction implicit finite-difference numerical technique (Peaceman and Rachford, 1955). The variations in temperatures result in density variations which represent a variation in the gravity over the region of interest. This variation is calculated and plotted.

### 2.1 Lithospheric Slab Translation

In the model presented by Minear and Toksoz (1970) movement of lithospheric material into the mantle is accomplished translation of temperatures ahead of the slab (see Minear and Toksoz (1970), Fig. 4). The material, as it is being subducted, is assumed to flow 'around the bend' in circular arcs. This method requires a linear interpolation procedure to determine the temperature values on the face of the slab as the slab bends downwards. Material assumed to be at a gridpoint may not stop at a

corresponding grid point on its 'journey' into the mantle over the period of time being considered, hence, the need for linear interpolation between grid points.

In the method presented here, the downward slab movement is carried out by translating the temperature values diagonally through the mesh as illustrated in Fig. 1(a). This is advantageous in that no interpolation is necessary. Also, different dip angles for the slab's descent may be readily accommodated by varying the relative lengths of  $\Delta x$  and  $\Delta z$  as shown in Figs. 1(b) and 1(c). This method can also conveniently provide for a change in the dip of the slab as illustrated in Fig. 1(c).

Comparison of the present model with that of Minear and Toksoz leads to considerations of the mechanism by which the slab begins to subduct and the nature of the interaction between the moving oceanic plate and the stable plate under which the slab is descending. Whereas the Minear and Toksoz model implies a bending of the slab by flexural slip with tensional stress at the top of the bend in the slab and compressional stress at the bottom of the bend, this model implies a downward slipping of the end of the slab together with local tension as it starts to subduct, essentially due to a normal faulting mechanism. Consider an initial steady-state lithosphere, becoming gravitationally unstable over lower density material: it will sag at first, creating a broad trench-like region on the ocean floor, followed by an inverted keystone failure at the axis of flexure. Successive



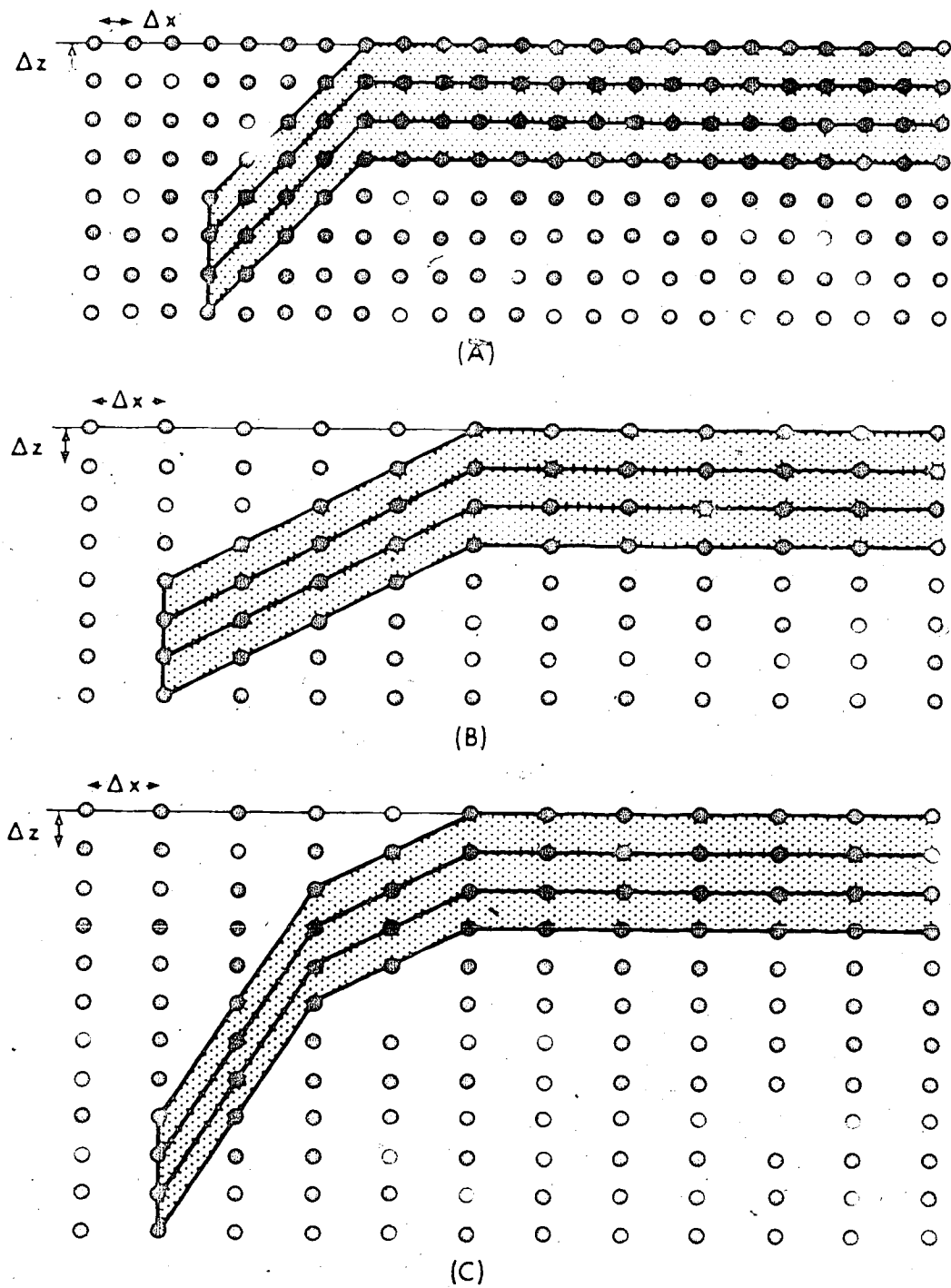


Fig. 1. Schematic representation of the translation procedure.  
 (A) large dip angle  
 (B) small dip angle  
 (C) change of dip angle with depth

normal faults will propagate into the slab, parallel to the first, permitting its end to descend into the mantle. The analogy can be made with a pack of cards sliding past one another. The stress-field at the top of the slab will necessarily be tectonic subparallel to the surface. Calculations done by Lliboutry (1969) indicate that the stresses involved in lithospheric sinking allow for a simple shear mechanism with normal faulting. This model maintains the vertical thickness of the lithosphere is unchanged with downward sinking of the plate in blocks by shearing along vertical planes.

This type of lithospheric descent is supported by first motion studies done by Isacks et al (1968) which indicate stress and deformation within a lithospheric plate may occur by normal faulting at shallow depths beneath the axis of the trench and landward of the uppermost zone. This type of normal faulting beneath the seaward slope of the oceanic trench is further supported by Katsumata and Sykes (1969) with studies done in the Phillipine Sea. Malahoff (1970) has concluded that gravity faulting is the dominant type of deformation in several trenches in the Pacific based on data obtained from seismic reflection profiles. Ludwig et al (1966) believes gravity faulting to be dominant in the Japan trench and Stauder (1968a, b) reached similar conclusions for the Aleutian trench. Lister (1971) obtained an acoustic reflection profile across the Chile trench off Valparaiso which showed downbowed reflections and normal faulting

indicating the lithospheric slab may be descending in an escalatorlike fashion. In terms of the probable history of the slab, the above translational procedure is believed to represent a possible mechanism for lithospheric movement in subduction zones.

#### 4.2 Temperature field computation

Calculation of the temperature field is accomplished using the Peaceman and Rachford alternating-direction implicit finite-difference method (Peaceman and Rachford, 1955) and the thermal energy balance equation:

$$C_p \rho \frac{\partial T}{\partial t} = \nabla \cdot (K \nabla T) + H \quad (1)$$

where  $C_p$  is the specific heat at constant pressure,  $\rho$  is the density,  $T$  is the temperature in degrees Celsius,  $K$  is the thermal conductivity and  $H$  is the heat generation per unit volume. Computation of the thermal regime proceeds as follows: temperatures representing lithospheric material are translated downwards as described in the previous section; the thermal energy balance equation is then employed to obtain the corresponding temperatures after a time  $\Delta t$ ; the lithospheric motion is then resumed and the temperatures recalculated; and so on. The vertical translation distance for the lithospheric slab is 10 km for each time step.

Use of the thermal energy balance equation is accomplished by expressing the equation in finite-difference form and using an algebraic scheme proposed by Thomas

(Peaceman and Rachford, 1955) and modified by Minear and Toksoz (1970) to obtain temperature solutions for each time step. The scheme requires setting up the derivatives to obtain temperature solutions solved implicitly in the x- and z-directions in alternate steps, resulting in the final solution. A comparison between the solutions obtained from the finite-difference method and an exact solution for the thermal energy balance equation indicates that the solutions agree to within a few percent (Toksoz et al, 1971).

Stability criteria established by Peaceman and Rachford (1955) indicate that the finite-difference solution is unconditionally stable for the thermal energy balance equation for the case of constant thermal conductivity. In other words, the scheme converges to the correct solution for all grid sizes and time steps. In the case of thermal conductivity being temperature dependent, the stability conditions have been established by Toksoz et al (1971) and Minear and Toksoz (1971). The stability conditions require that the spatial derivatives in thermal conductivity be restricted in magnitude to allow convergence of the scheme to the proper solution. In all examples presented, the convergence requirements have been met.

### 2.3 The Initial and Boundary Conditions

The boundary conditions are similar to those employed by Minear and Toksoz (1970). Heat flux into the bottom of the grid was taken as constant to maintain steady-state

conditions in the mantle. The surface of the earth is maintained at 0°C and it is assumed that there is no heat flux across the side boundaries of the region. This latter condition implies that the edges of the region of interest are not affected by the downgoing slab. The density distribution used in the calculations closely follows the Bullen A density curve and is shown in Fig. 2.

The initial vertical temperature distribution was obtained using the relationship given by Mercier and Carter (1975) for low-temperature oceanic pyroxene geotherms:

$$T = 4.34(P+8.6) - 11840/(P+8.6) + 1340 \quad (2)$$

where  $T$  is the temperature in degrees Celsius and  $P$  is the pressure in kilobars (where  $P$  follows the normal hydrostatic gradient). Small variations in the initial temperature distribution are unimportant since it is of interest in this model to study perturbations in the thermal regime. Also, there is much uncertainty in the exact mantle geotherm as illustrated by the variety of geotherms published (Mercier and Carter, 1975).

The specific heat at constant pressure is taken as constant and given the value  $C_p = 1.3 \times 10^7$  ergs/gm (Toksoz et al, 1971). For comparisons with the linear and Toksoz method the thermal conductivity used is given by MacDonald (1959), which includes constant lattice conductivity plus a radiative transfer term which is dependent upon temperature. This thermal conductivity gives unrealistic values for

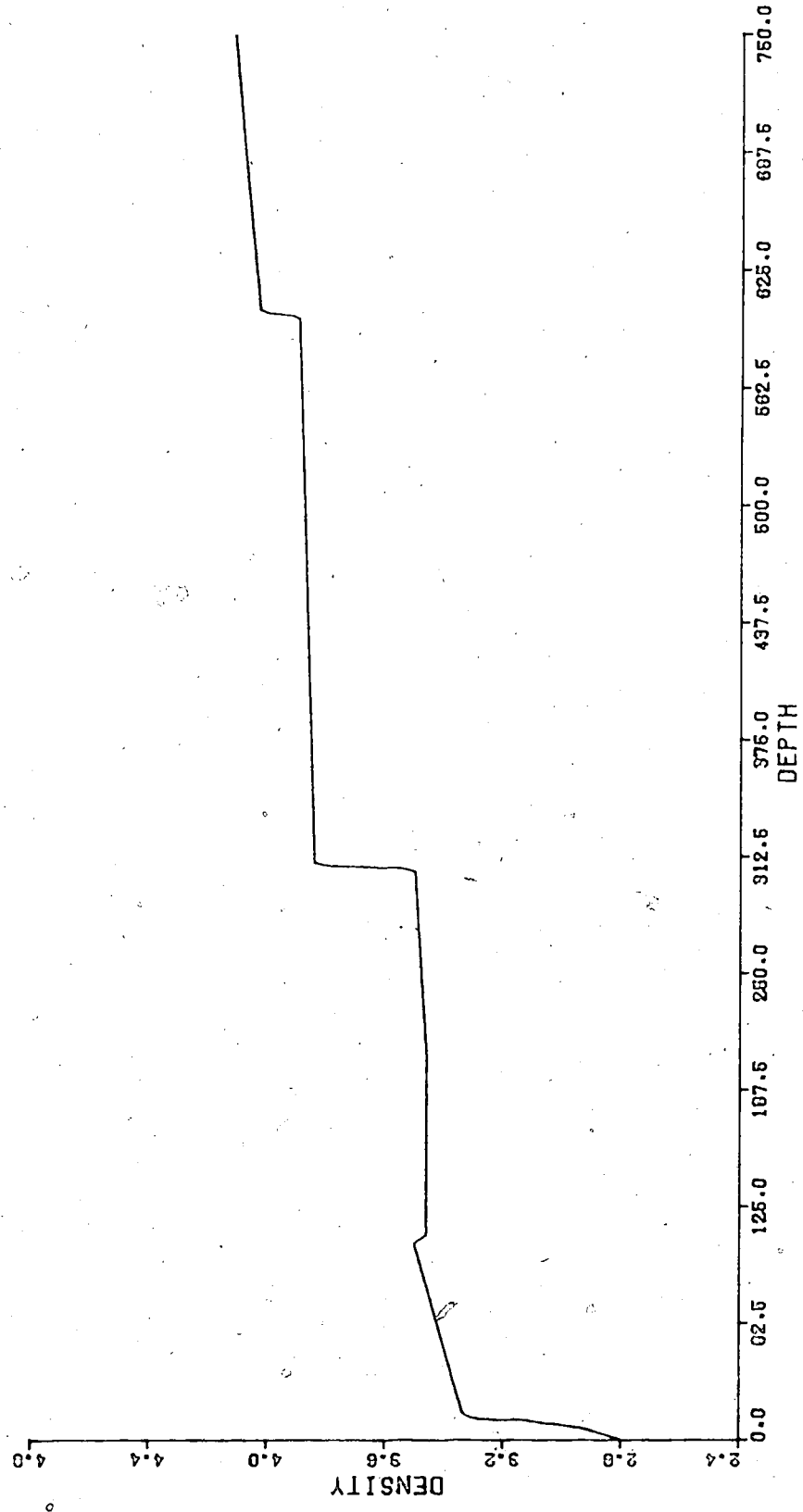


Fig. 2. The variation of density with depth. The density is in units of gm/cm<sup>3</sup> and depth is in units of kilometers.

temperatures above 1000°C and will therefore affect the temperature distribution within the descending slab (Turcotte and Oxburgh, 1972). Furthermore, experimental evidence indicates the radiative opacity of olivine increases with temperature (Aronson et al., 1970). Therefore, for most models a constant conductivity is used with a value of  $K = .01 \text{ cal/cm-sec}^\circ\text{C}$  (Hasebe et al, 1970).

#### 2.4 Heat Sources

The inclusion of heat source coefficients is incorporated through the heat production term in the thermal energy balance equation. Heat sources which have been included are those due to adiabatic compression and shear-strain heating. Heating due to radiogenic sources has not been included since it is expected the effect will be minimal<sup>o</sup> in the time periods considered. This has been supported by calculations done by Minear and Toksoz (1970) and Toksoz et al (1971). Heating due to phase changes within the descending slab is of no known importance for depths less than 300 km and has not been considered because of the uncertainty in the contribution this term has in the temperature field computation. Calculations done by Oxburgh and Turcotte (1970) indicate the effect of phase changes is insignificant on the thermal regime.

The heating of the lithosphere as it descends into the mantle due to compression is calculated by the rate of energy release at depth  $h$  (Toksoz et al, 1971; Hanks and

Whitcomb, 1971):

$$\left. \frac{dQ}{dt} \right|_h = C_p \rho \frac{\partial T}{\partial t} = C_p \rho \frac{\partial T}{\partial z} V_z = \rho g \alpha T V_z \quad (3)$$

where  $\rho$  is the density,  $C_p$  is the specific heat at constant pressure,  $V_z$  is the vertical velocity of the slab,  $g$  is gravity and  $T$  is the temperature. The volume coefficient of expansion is assumed to have a depth dependence given by:

$$\alpha = \exp(3.58 - 0.0072z) \quad (4)$$

with the depth  $z$  in kilometers and  $\alpha$  in units of  $10^{-6}/^{\circ}\text{C}$ .

The inclusion of a shear-strain heating term is constrained geologically by the need to create partial melt at the upper surface of the downgoing slab (Hatherton and Dickinson, 1969). Several shear-strain coefficients were employed in order to determine if partial melt was produced for the different subduction velocities. Shear heating was included along the upper surface of the slab and also along the bottom edge of the slab. To estimate the effect of shear-strain heating, assuming viscous dissipation:

$$\dot{E} = \sigma \dot{\epsilon} = \eta \left( \frac{\partial v}{\partial \xi} \right)^2 \quad (5)$$

where  $\sigma$  is the stress,  $\dot{\epsilon}$  is the strain rate,  $\eta$  is the viscosity, and the velocity gradient  $\left( \frac{\partial v}{\partial \xi} \right)$  is taken perpendicular to slab motion, across the shear zone. If we assume the velocity distribution across the shear zone varies linearly as:

$$v(\xi) = v_0 \frac{\xi}{T} \quad \xi < T \quad (6)$$



where  $v_0$  is the slab velocity,  $T$  is the width of the shear zone and  $l$  is measured across the shear zone, the rate of viscous dissipation is then:

$$\dot{E} = \eta \left( \frac{v_0}{T} \right)^2 \quad (7)$$

According to theoretical calculations (T. Spanos, private communication) the shear zone is approximately 10 km wide. Therefore, the viscosity of the shear zone may be estimated if the amount of shear heating needed to produce partial melt is known.

## 2.5 Rising Melt.

The model may be adapted to study the effect of generating melt along the upper surface of the downgoing slab and causing it to rise. This simulates rising diapiric material when it has reached a stage of partial melting at the top edge of the slab, i.e. when the geotherm has intersected the solidus curve for basalt. The solidus for basalt was taken from Yoder and Tilley (1962) with a gradient of 3°C/km. Geological studies indicate that basalt magma is generated along the upper surface of the slab and this magma undergoes crystal fractionation forming andesitic magma near the earth's surface (Hatherton and Dickinson, 1969; Kuno, 1968). Therefore, simulating upward movement of basalt magmas is a good approximation geologically.

To simulate movement of magma from the upper surface of the descending slab temperatures are translated upwards in a

similar manner to movement of lithospheric material downwards. The rising material is assumed to have a velocity of 1 cm/year to maintain order of magnitude energy balance between heat being produced in the shear zone and the amount of heat removed. The amount of heat being removed may be estimated by (Hasebe et al, 1970):

$$Q = C \cdot V \cdot \Delta T \quad (8)$$

where  $C$  is the specific heat at constant volume,  $V$  is the velocity of the rising material and  $\Delta T$  is the temperature difference between the top and bottom of the magma layer. No allowance has been made for heat of fusion as the amount of heat required is about two orders of magnitude lower than the amount of heat produced, minimizing the effect of heat absorption due to heat of fusion.

## 2.6 Gravity Calculations

The gravity effect of a sinking slab is calculated using a method developed by Dyrelus and Vogel (1971). For a two-dimensional rectangular block with upper edge at the surface  $z=0$ , the gravity effect is given by:

$$\Delta g = \nu \rho \left( a \ln \frac{a^2 + z^2}{a^2} - b \ln \frac{b^2 + z^2}{b^2} + \theta z \left( \tan^{-1} \frac{a}{z} - \tan^{-1} \frac{b}{z} \right) \right) \quad (9)$$

where  $\nu$  is the gravitational constant,  $\rho$  is the density,  $x_1$  is the x-coordinate of the left edge of the block,  $x_2$  is the x-coordinate of the right edge of the block,  $a$  is  $x - x_1$ ,  $b$  is  $x - x_2$  and  $z$  is the depth to the lower edge of the block.

The above equation also holds for the upper corners of the block. When  $x=x_1$ ;

$$\lim_{a \rightarrow 0} \left( a \ln \frac{a^2 + z^2}{a^2} \right) = 0 \quad (10)$$

and therefore:

$$\Delta g_{a=0} = \nu \rho \left( -b \ln \frac{b^2 + z^2}{b^2} + 2z \tan^{-1} \frac{b}{z} \right) \quad (11)$$

For  $x=x_2$ :

$$\Delta g_{b=0} = \nu \rho \left( a \ln \frac{a^2 + z^2}{a^2} + 2z \tan^{-1} \frac{a}{z} \right) \quad (12)$$

If the gravity effect is considered from the  $j^{\text{th}}$  block at the  $i^{\text{th}}$  point of observation, the total gravity effect at the point of observation  $P_i$  is:

$$g_i = \sum_{j=1}^m \Delta g_{ij} \quad (13)$$

where there are 'm' blocks.

For the calculation of the gravity effect a two-dimensional grid was used which incorporated the densities used in the thermal regime computation. A system of grid cells was established which used densities specified at the four grid points enveloping a grid cell. The gravity contribution from each grid cell was then added to obtain the gravity effect at selected observation points at the surface.

Variations in density that are accounted for in this calculation are due to temperature fluctuations in the lithosphere and surrounding mantle. The changes in density

include the effect of the volume coefficient of expansion for temperature above and below the normal mantle geotherm. It is expected that the cold sinking slab will maintain a higher density than the surrounding material and partially molten material will be less dense than the surrounding medium. No allowance has been made for density variations due to phase changes and chemical inhomogeneities.

## CHAPTER 3 THERMAL REGIMES FOR DOWNGOING SLABS

### 3.1 Comparison of the Diagonal Translation method and the Minear and Toksoz Method

In order to compare the diagonal translation method with the Minear and Toksoz interpolation procedure, a slab with a dip angle of  $45^\circ$  was modelled using both techniques. A slab 80 km thick superimposed on a grid of  $151 \times 151$  points is used, in which the mesh size is taken as 5 km x 5 km. The slab moves with a vertical velocity of 1.4 cm/year, and so the velocity of the slab through the surrounding material is 2.0 cm/year.

The two models are compared in Figs. 3-5. The left sides of the figures show the results for the Minear and Toksoz method (Figs. 3A, 4A and 5A), while the right sides show the effects of the diagonal translation procedure (Figs. 3B, 4B and 5B). The temperature fields are shown in the lower diagrams with the corresponding heat flow profiles shown at the top of the figures. Figure 3 shows the thermal regime and surface heat flow at 10.63 million years after the start of subduction, while Figs. 4 and 5 are at 21.26 million years and 35.44 million years, respectively, after the beginning of subduction.

From the figures the effect of the narrower slab in the diagonal translation procedure is apparent in that the isotherms lie closer together inside such a slab. This



Fig. 3. Comparison of the diagonal translation procedure with the circular arc translation procedure. The results are for 10.63 million years after the start of subduction. The heat flow units are in  $\mu\text{cal}/\text{cm}^2\text{-sec}$  and temperature values are in  $^{\circ}\text{C}$ .

A: circular arc procedure.  
 B: diagonal translation procedure.

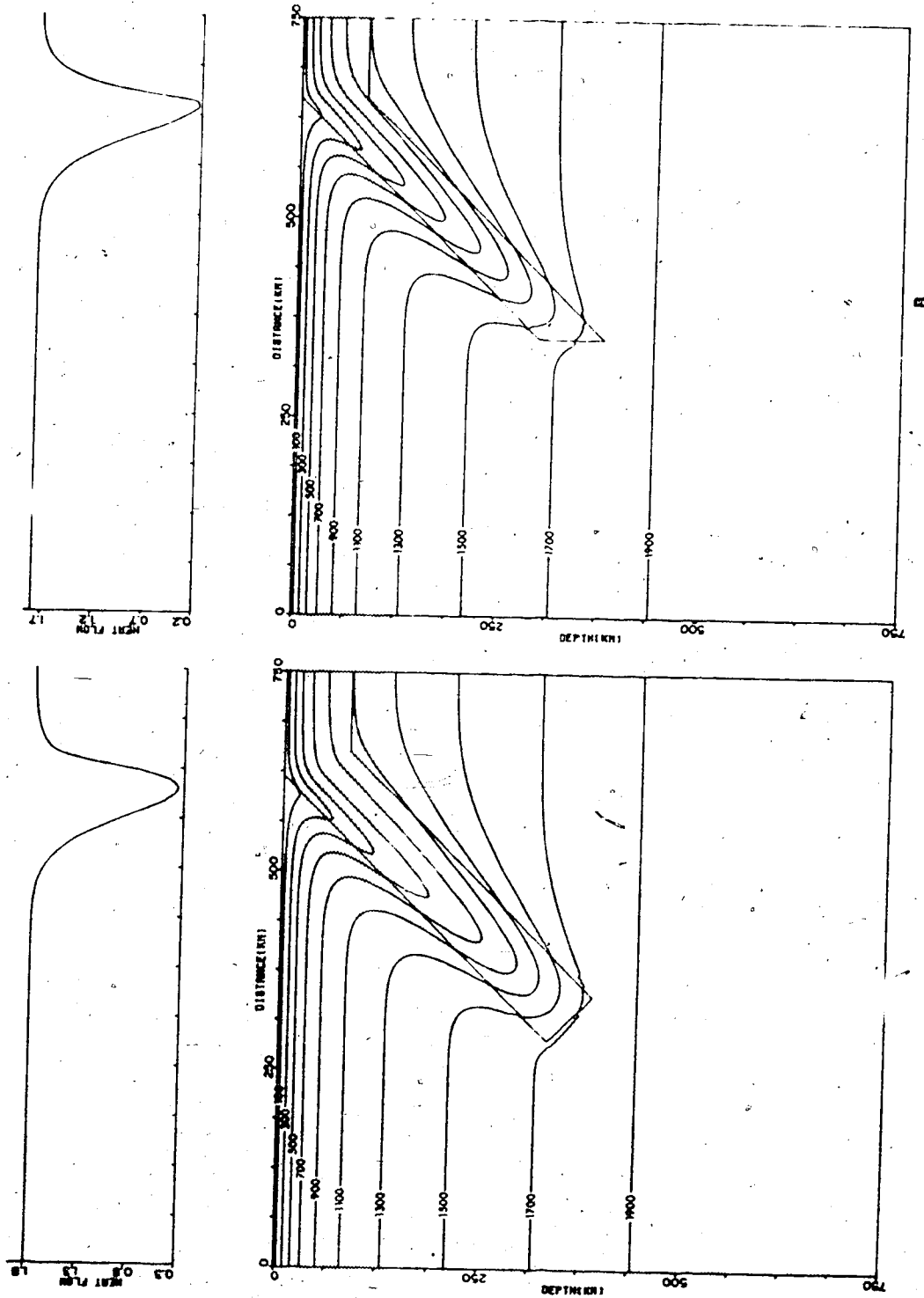


Fig. 4. As Fig. 3, but at 21.26 million years.

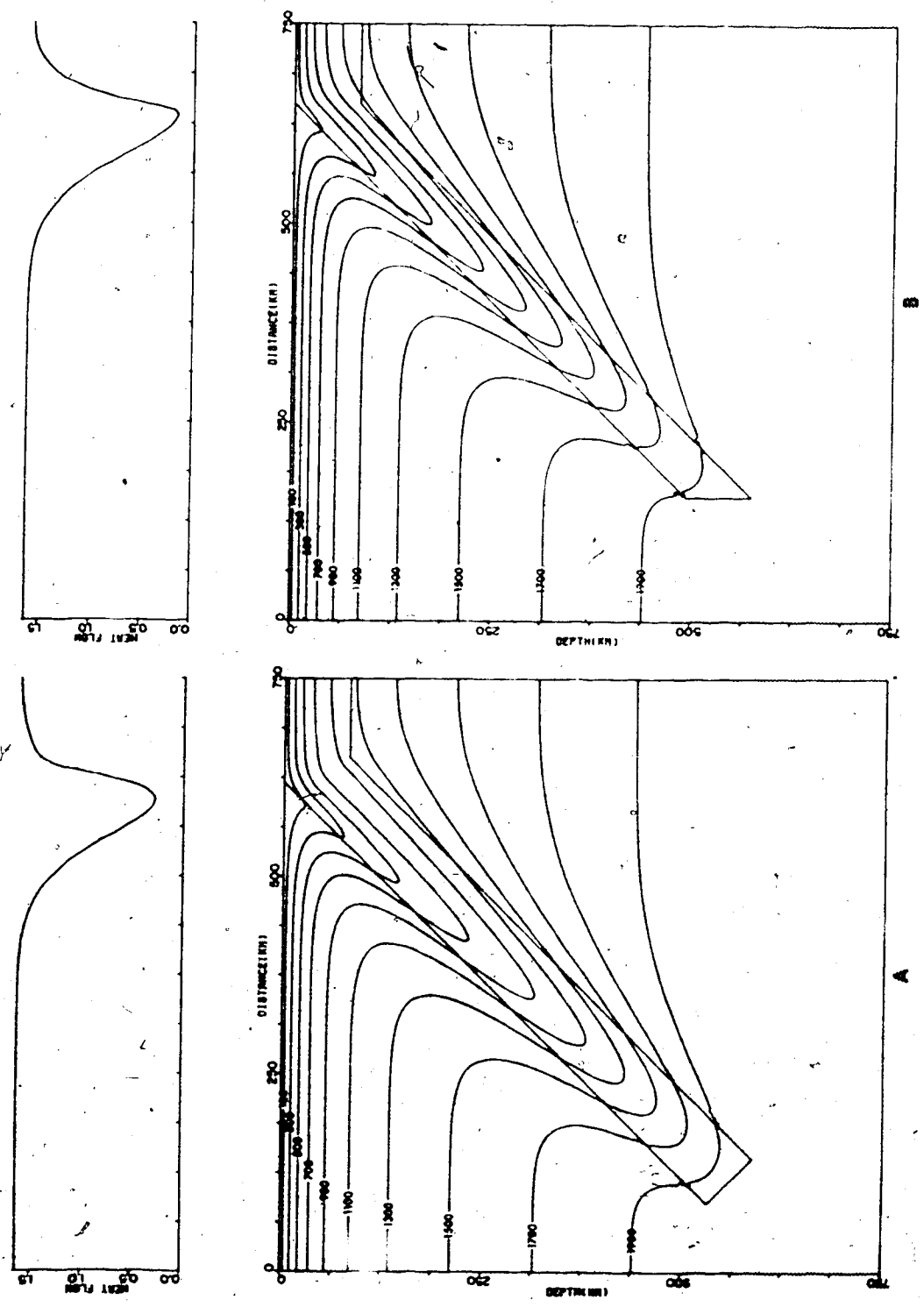


Fig. 5. As Fig. 3, but at 35.44 million years.



implies that the distortion of the normal geothermal field by the cool downgoing slab depends on the thickness of the slab, and the perturbation of the thermal regime throughout the surrounding material takes place slowly. Also, the effect of the vertical lower face of the slab in the diagonal translation procedure is evident, causing distortion of the isotherms near this region. Although the isotherms differ to some extent near the bottom of the slab, the temperature field above the slab is not greatly affected except near the surface. Close inspection of Fig. 3 shows that the isotherms are slightly different near the surface close to the point where subduction begins. This is particularly true for the 100°C isotherm. This difference is also apparent in Figs. 4 and 5. The surface heat flow values reflect this near surface difference and it appears that the minimum in the heat flow is lower in the diagonal translation method. This difference becomes more apparent as time goes on (Figs. 4 and 5) and the minimum for the diagonal translation method is noticeably lower at 35.44 million years.

The reason for the lower minimum becomes apparent when the geometry of the two subducting mechanisms is considered. In the Minner and Toksoz method where material is assumed to flow 'around the bend', the actual vertical motion of the material is not as pronounced near the surface of the lithosphere as in the diagonal translation procedure. The 'bending' phenomenon allows the slab to traverse a larger

horizontal distance in the Minear and Toksoz method, producing smaller temperature gradients near the surface of the slab and thus allowing the near surface portion of the slab to warm up at a quicker rate. The effect also causes the heat flow profiles to differ as time proceeds, particularly to the right of the point where subduction begins (as in Figs. 3, 4 and 5).

### 3.2 Thermal Regimes for Slabs with Different Dip Angles

The model was used to investigate the temperature fields and heat flow profiles associated with a shallower dip angle and with a slab in which the dip angle changes with depth. The thermal conductivity used in these models is given by MacDonald (1959).

#### 3.2.1 Dip Angle of 26.6°

The results for a slab in which the dip angle is 26.6° are shown in Figs. 6-8. In this model  $\Delta x=10$  km and  $\Delta z=5$  km. The vertical velocity of the slab is 1.4 cm/year and therefore the subduction velocity is 3.2 cm/year. Figures 6-8 show the associated thermal fields and surface heat flow profiles of 10.63, 21.26, and 35.44 million years, respectively, after the start of subduction. Comparison of this shallower angle with the 45° angle of Figs. 3-5 shows the isotherms more severely distorted for the 26.6° dipping case. This is explained by the greater subduction velocity in the shallower dipping case. The 26.6° dipping slab does

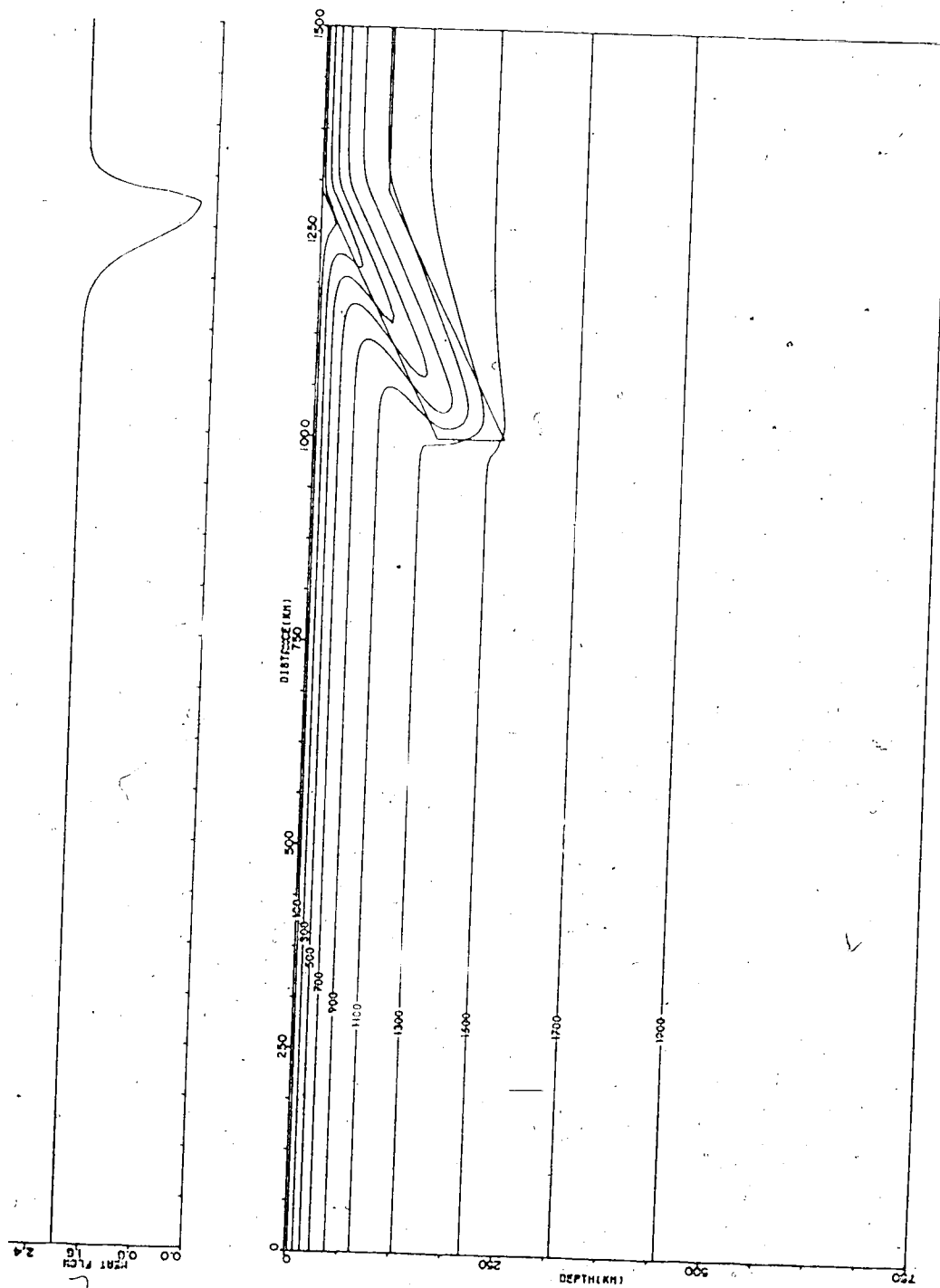


Fig. 6. The temperature regime and surface heat flow profile for a subducting slab with dip angle  $26.6^\circ$  at 10.63 million years after the start of subduction.



Fig. 7. As Fig. 6, but at 21.26 million years.

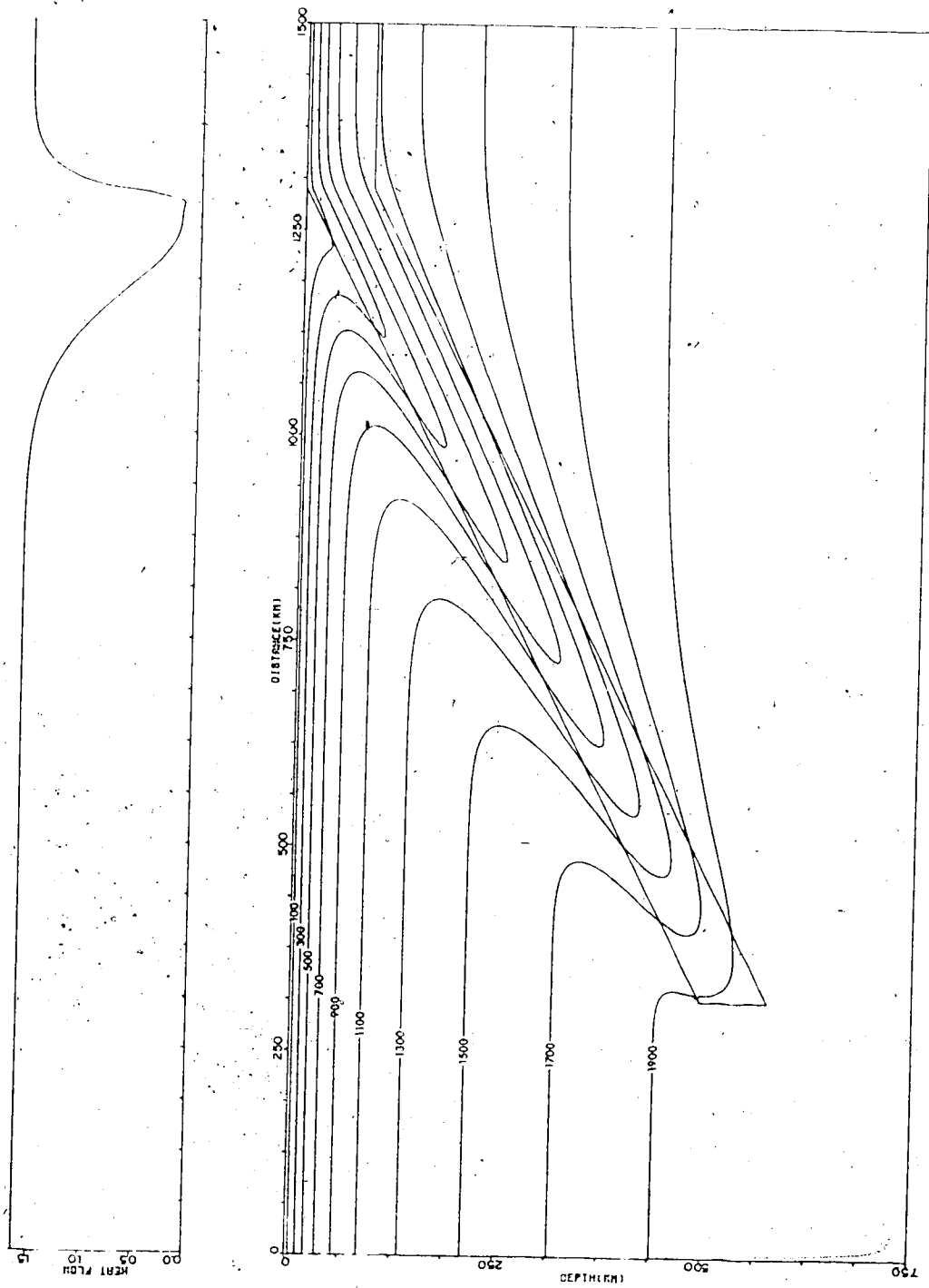


Fig. 8. As Fig. 6, but at 35.44 million years.

not have as much time to warm up as the 45° case, resulting in isotherms being taken to greater depths. Also, the shallower dipping slab has a larger thickness in the direction of subduction, resulting in a thermal boundary layer which requires a greater time to be heated to mantle temperatures.

Although the 45° dipping slab in Figs. 3-5 has a fairly symmetric heat flow profile, the 26.6° dipping slab has an asymmetric form which becomes more pronounced as subduction progresses. Further, near the point where subduction begins, the bottom of the dip in the heat flow becomes flatter as time progresses (Figs. 6-8). This result is apparent from the form of the downwarping mechanism and the rate of subduction. Whereas the horizontal slab velocity in the 45° case is 1.4 cm/year, the horizontal velocity in the 26.6° case is 2.8 cm/year resulting in a broad minimum in the heat flow pattern.

### 3.2.2 Dip Angle Which Changes with Depth

To investigate the temperature fields of slabs in which the dip angle changes with depth, two models were run. The first model is that of a slab which dips initially at 26.6° and after 10.63 million years the dip angle changes to 45°. The second model also initially dips at 26.6°, but after 10.63 million years the dip angle changes to 56.3°. In both models the downgoing velocity of the material in the 26.6° portion is 3.2 cm/year. In the lower portions of the slabs

the subduction velocity is 4.0 cm/year for the 45° slab and 5.1 cm/year for the 56.3° slab.

Figures 9 and 10 give results for these two models at 21.26 million years after the beginning of subduction. By comparing Figs. 9 and 10, it is seen that the slab has penetrated deeper into the mantle in Fig. 10 for the same time period, resulting in the isotherms being pulled down further into the mantle with the steeper dipping slab. The lowering of the isotherms can also be interpreted as due to the greater subduction velocity in the steeper dipping slab. Near the point where subduction begins the heat flow profiles and thermal regimes are similar. This implies that the perturbations created at greater depths do not affect the thermal regimes near the surface. When compared with the slab with constant 26.6° dip angle (Fig. 7) there is little difference between the surface heat flow profiles, although the temperatures near the slabs display marked differences deeper in the mantle. These results indicate that the perturbations in the thermal fields at depth do not have sufficient time to be propagated to the surface in the time periods considered, giving little information regarding slab processes related to heat conduction and slab velocity changes at depth.

### 3.3 Thermal Regimes for Slabs with Heat Sources

In the examples presented here heat conduction along with the inclusion of heat source coefficients for shear-

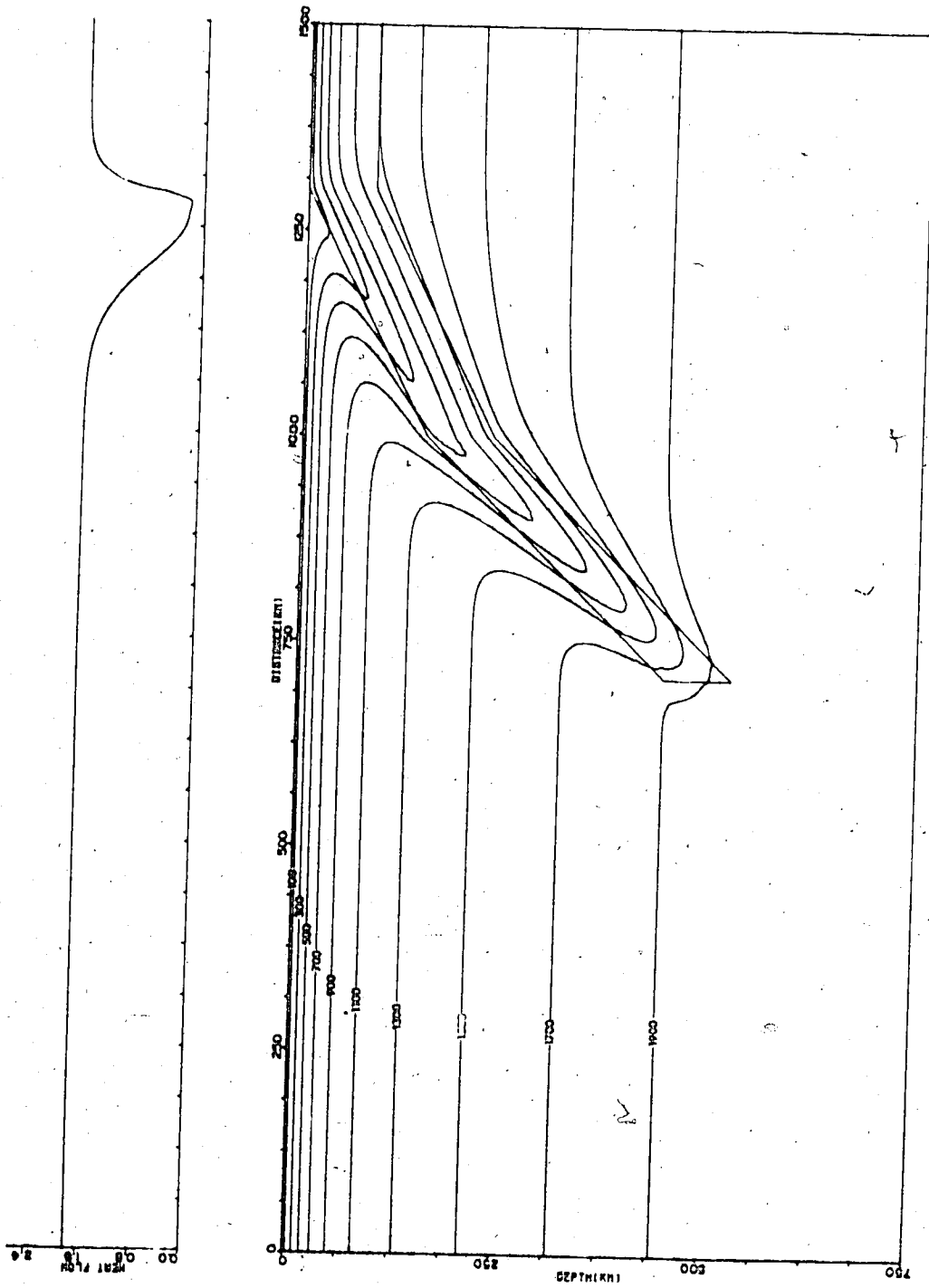


Fig. 9. A downgoing slab with dip angles  $26.6^\circ$  and  $45.0^\circ$ .





Fig. 10. A downgoing slab with dip angles  $26.6^\circ$  and  $56.3^\circ$ .

strain heating and adiabatic compression are considered. The model was used to compare thermal regimes and heat flow profiles associated with slabs dipping at  $26.6^\circ$  and  $45^\circ$  for two vertical subduction velocities,  $0.7$  cm/year and  $5.6$  cm/year.

### 3.3.1 Subduction Rate of $0.7$ cm/year

The results for a downgoing slab with dip angle  $45^\circ$  and a slab with dip angle  $26.6^\circ$  are shown in Figs. 11-13. Figure 11 illustrates the thermal regime and surface heat flow profile associated with a slab dipping at  $45^\circ$  with a vertical velocity of  $0.7$  cm/year. The resulting subduction velocity is  $1.0$  cm/year. Adiabatic compression is considered as a heat source within the slab together with a shear-strain heating coefficient of  $1.6 \times 10^{-4}$  ergs/cm<sup>3</sup>-sec along the top edge of the slab and  $1.6 \times 10^{-5}$  ergs/cm<sup>3</sup>-sec along the bottom edge of the slab. The order of magnitude lower shear heating term along the bottom edge of the slab is due to an assumed smaller viscosity in the low velocity zone in the mantle (Schubert et al., 1976). The shear zones along the top and bottom edges of the slab are assumed to have a  $10$  km vertical thickness. Together with the assumed values of shear heating, this implies an average viscosity in the shear zone along the upper edge of the slab of approximately  $10^{23}$  poise. This agrees within an order of magnitude with the average viscosity in the shear zone if the descending lithosphere is assumed to have a viscosity of between  $10^{22}$

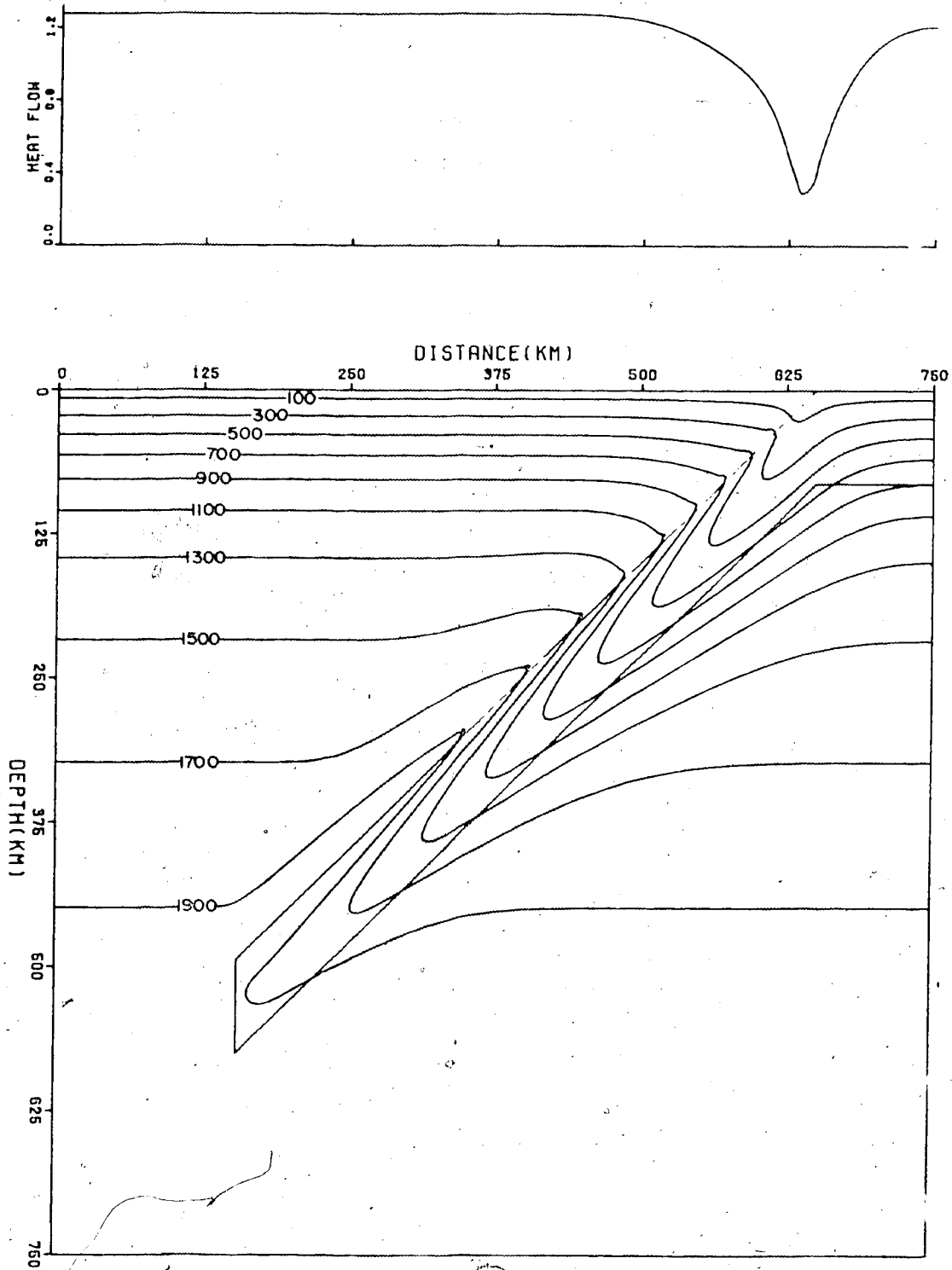


Fig. 11. The temperature regime and surface heat flow profile for a descending slab with a dip angle of  $45^\circ$  at 70.88 million years after the start of subduction. Adiabatic compression and shear heating are included as heat sources. The slab velocity is 10 cm/year.

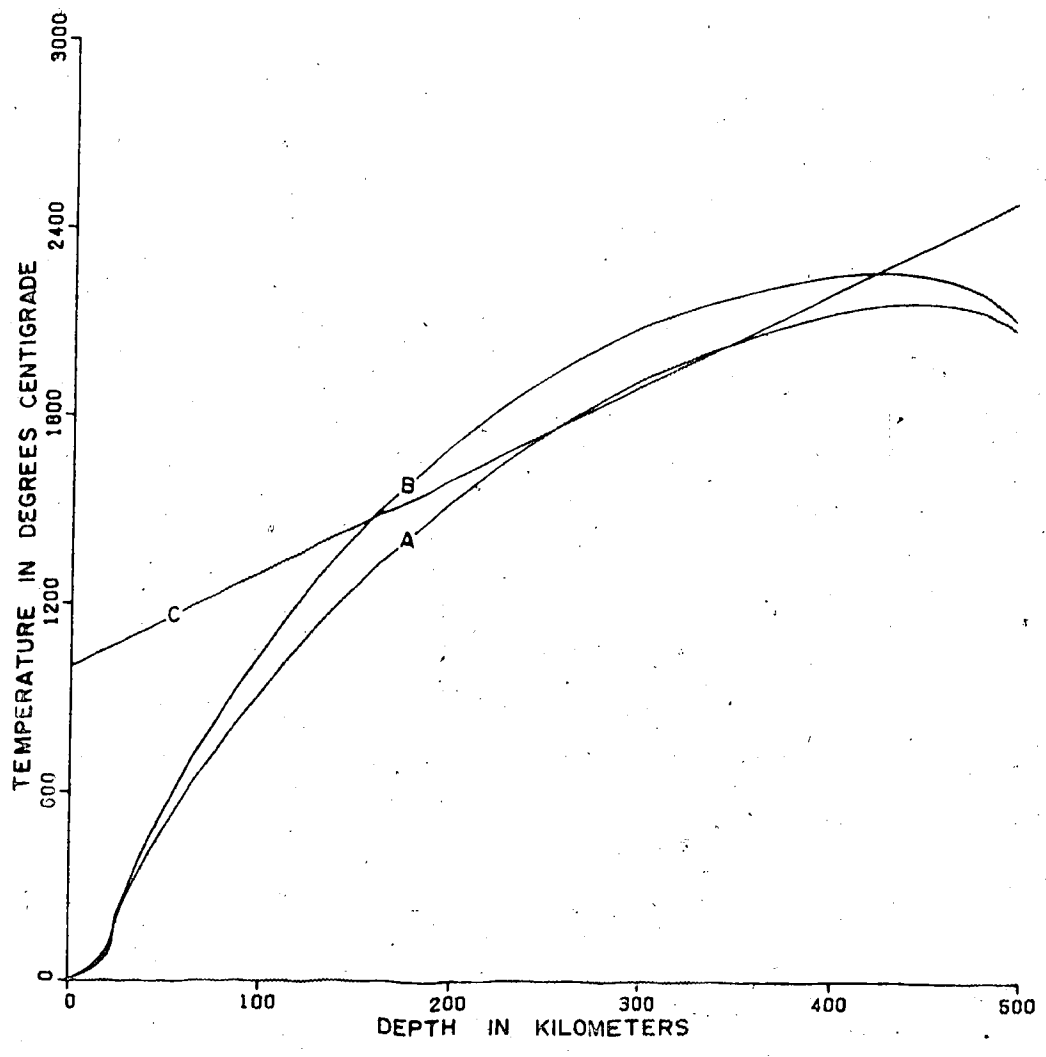


Fig. 12. Temperature-depth profiles along the upper surface of the slab for the models of Fig. 11 (curve A) and Fig. 13 (curve B).

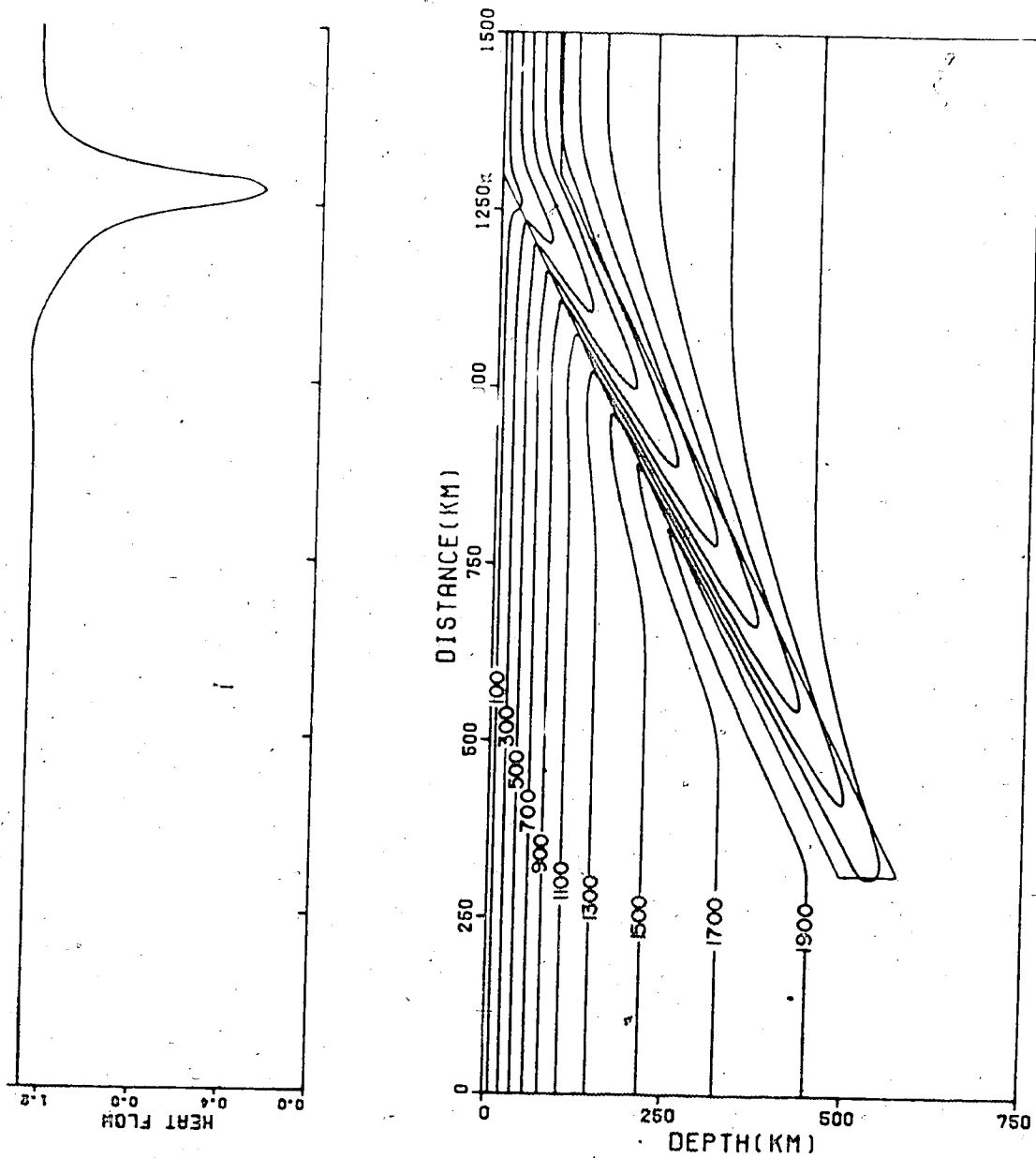


Fig. 13. As Fig.11, but with a dip angle of  $26.6^\circ$  and a slab velocity of 1.6 cm/year.

poise to  $10^{25}$  poise (Walcott, 1970; De Braemacker, 1977) and the upper mantle has a viscosity of approximately  $10^{21}$  poise (Schubert et al, 1976). Results for a total subduction period of 70.88 million years are illustrated in Figs. 11-13. Figure 12 (curve A) gives a temperature-depth profile along the upper surface of the slab. This may be compared with Fig. 12 (curve C) which represents the solidus for basalt (Yoder and Tilley, 1962).

From Fig. 11 it is seen that the interior of the slab remains cooler than the surrounding mantle to depths greater than 500 km implying that the slab does not reach thermal equilibrium in the time period considered. This may be justified by the fact that earthquakes occur to depths of 700 km within the downgoing slab [Benioff, 1954; Isacks et al, 1968] a possible source of earthquakes may be due to a colder brittle slab descending into the mantle (Griggs, 1972; McKenzie, 1969). The shear-strain heating term raises the isotherms locally near the top edge of the slab although the bottom edge of the slab is unaffected by shear heating. The surface heat flow pattern exhibits a distinct low near the point of subduction with no visible change in the heat flow as a result of shear heating along the upper surface of the slab. This result indicates that a thermal pulse propagating from the upper surface of the slab will not reach the surface in the time period considered. Temperatures along the upper surface of the slab intersect the melting curve between the depths of 250 km and 350 km

implying that melt is generated in this region.

The thermal regime and surface heat flow profile for a slab dipping at  $26.6^\circ$  are illustrated in Fig. 13. The subduction velocity is 1.6 cm/year and the heat sources are the same as those of Fig. 11. Total time of subduction is 70.88 million years. Fig. 12 (curve B) gives the associated temperature-depth profile along the upper surface of the slab indicating that temperatures along the upper edge of the slab reach the partial melt curve from approximately 150 km to 400 km depth.

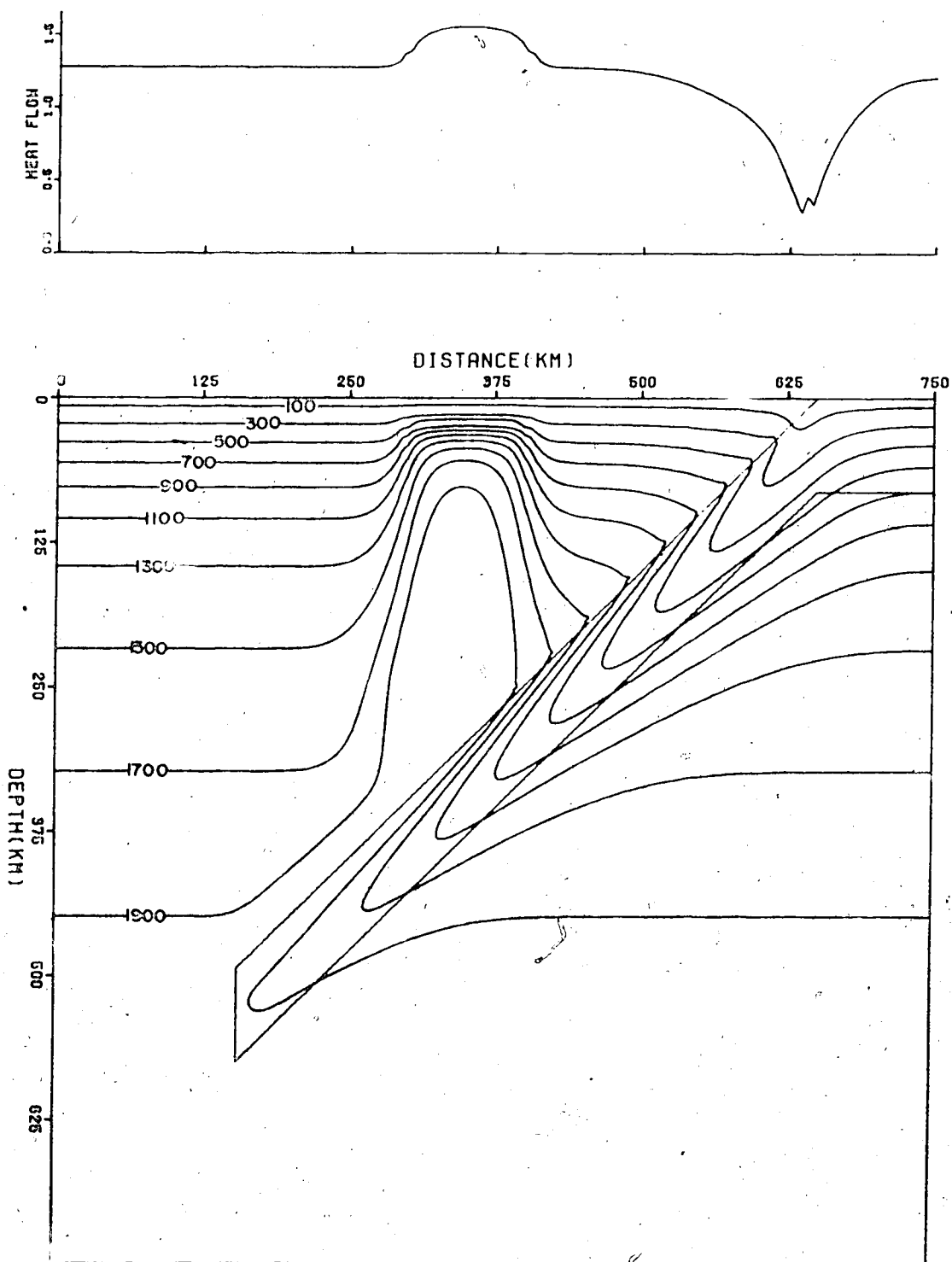
A comparison of the results for the two different dip angles indicates that the interior and lower parts of the slab remain cooler at shallower angles of dip due to the greater subduction velocity for the shallower angle slab and the greater thickness of this slab resulting from the descent mechanism. The upper surface of the slab is maintained at higher temperatures in the shallower dipping slab due to increased shear zone thickness because, in turn, of the increased slab thickness at shallower dips. Melting then occurs at shallower depths. The slightly larger subduction velocity in the  $26.6^\circ$  slab tends to cause a general lowering of the isotherms within the slab region although the effect is largely negated along the slab's upper surface due to the increased shear zone thickness. There is little indication in the surface heat flow of the presence of shear heating in either of the slabs, although the dip in the heat flow profiles may be more symmetric as a

result of shear heating (induced artificially by the depth at which shear heating begins in this model: 30 km).

The effect of generating melt and causing it to rise is shown in Figs. 14-15. For both a  $45^\circ$  dipping slab and  $26.6^\circ$  dipping slab containing the same heat sources as shown in Figs. 11 and 13, melt was forced to rise for depths extending from 250 km to 350 km. This simulates rising diapiric material after it has reached the basalt solidus along the top edge of the slab. The region of rising melt extends from the 300 km point to the 400 km point along the horizontal axis in Fig. 14 and from the 600 km point to the 800 km point along the horizontal axis in Fig. 15. The region of rising partial melt is in agreement with studies done by Hatherton and Dickinson (1969) on the relationship between the depth of the shear zone below volcanoes in relation to the distance of the volcanoes from the trench axis. A list of a number of volcanoes in relation to trench systems is shown in Table 1 (Hatherton and Dickinson, 1969).

For the  $45^\circ$  dipping slab the result of the melting anomaly is to increase the heat flow by approximately 25% at 300 km from the point of subduction. There is a general raising of the geotherms in the melt region due to the rising material with a large temperature gradient occurring at approximately 30 km depth. Temperatures throughout the melt region remain high compared with the surrounding mantle. Also, the width of the heat flow anomaly corresponds with the width of the melting anomaly resulting from the





14. Temperature regime and surface heat flow profile for a 45° dipping slab with rising melt. Heat sources are the same as in Fig. 11.

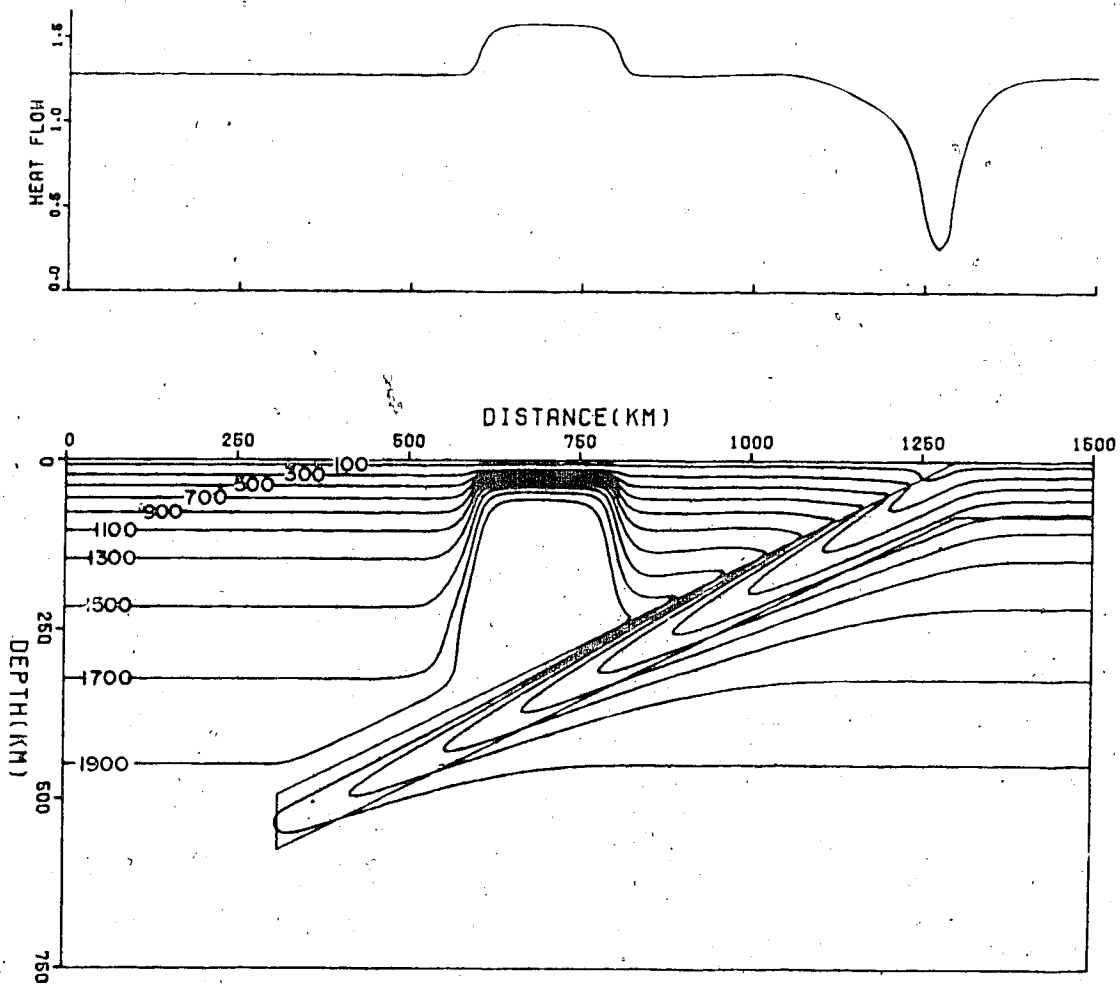


Fig. 15. As Fig. 14, but with a dip angle of  $26.6^\circ$ .

Table 1. Geometry of Active Volcanoes  
in Indonesia, Lesser Antilles and  
New Zealand

<u>Indonesia</u>	<u>No.*</u>	<u>h<sub>a</sub> : km</u>	<u>d<sub>a</sub> * km</u>
(21) Marapi	6,1-14	160	320
(22) Tandikat	6,1-15	130	300
(23) Galunggung	6,3-14	130	270
(24) Tjeremaf	6,3-17	210	320
(25) Slamet	6,13-18	210	-
(26) Dieng	6,3-20	260	330
(27) Ungaran	6,3-23	290	-
(28) Merapi	6,3-25	225	-
(29) Paluweh	6,4-15	240	-
(30) Lewotolo	6,4-23	240	-
(31) Lokon-Empung	6,6-10	130	-
(32) Dukono	6,8-1	180	-

Lesser Antilles

(33) Mt. Hisery	16-3	120	250
(34) Nevis Peak	16-4	120	250
(35) Montserrat	16-5	120	250
(36) Mont Pelee	16-12	130	-
(37) Qualibou, St. Lucia	16-14	130	-

New Zealand

(38) Ohakune-Edgecumbe	-	140	300
(39) White Island	-	210	300
(40) Egmont	-	280	380

\* Number of volcanoes in Catalogue of the Volcanoes of the World [1951, 1961].

: depth to center of Benioff zone below volcano

\* distance to volcano from centre of trench, where present.

vertical transport of magma (and therefore heat) towards the earth's surface. Figure 15 shows the melting anomaly in the  $26.6^\circ$  dipping case rising from the same depths as those of Fig. 14. Due to the revised grid dimensions for the  $26.6^\circ$  dipping slab, the region of partial melting is widened along the horizontal axis. Heat flow is also raised by approximately 25% over the width of the anomaly. The region of high heat flow is in agreement with heat flow measurements in the Japan Sea (Vacquier et al, 1966) which indicate that the width of the heat flow anomaly in the island arc region is dependent on the dip angle of the fault zone below the island arc. A corresponding high heat flow anomaly over a shallow dipping slab (approximately  $30^\circ$  dip) has twice the horizontal width as compared with a steeper dipping slab (approximately  $45^\circ$ ). This result may indicate that the corresponding heat flow anomaly due to partial melting may be caused by melt created in a specific depth interval not related to the dip angle of the slab.

### 3.3.2 Subduction Rate of 5.6 cm/year

The results for a downgoing slab with a vertical velocity of 5.6 cm/year are shown in Figs. 16-19. In the  $45^\circ$  dipping slab of Fig. 16, the subduction velocity of the slab is 8.0 cm/year. This represents an upper limit for the spreading rate of the lithosphere (Le Pichon et al, 1973). Total time of subduction is 8.86 million years and heat

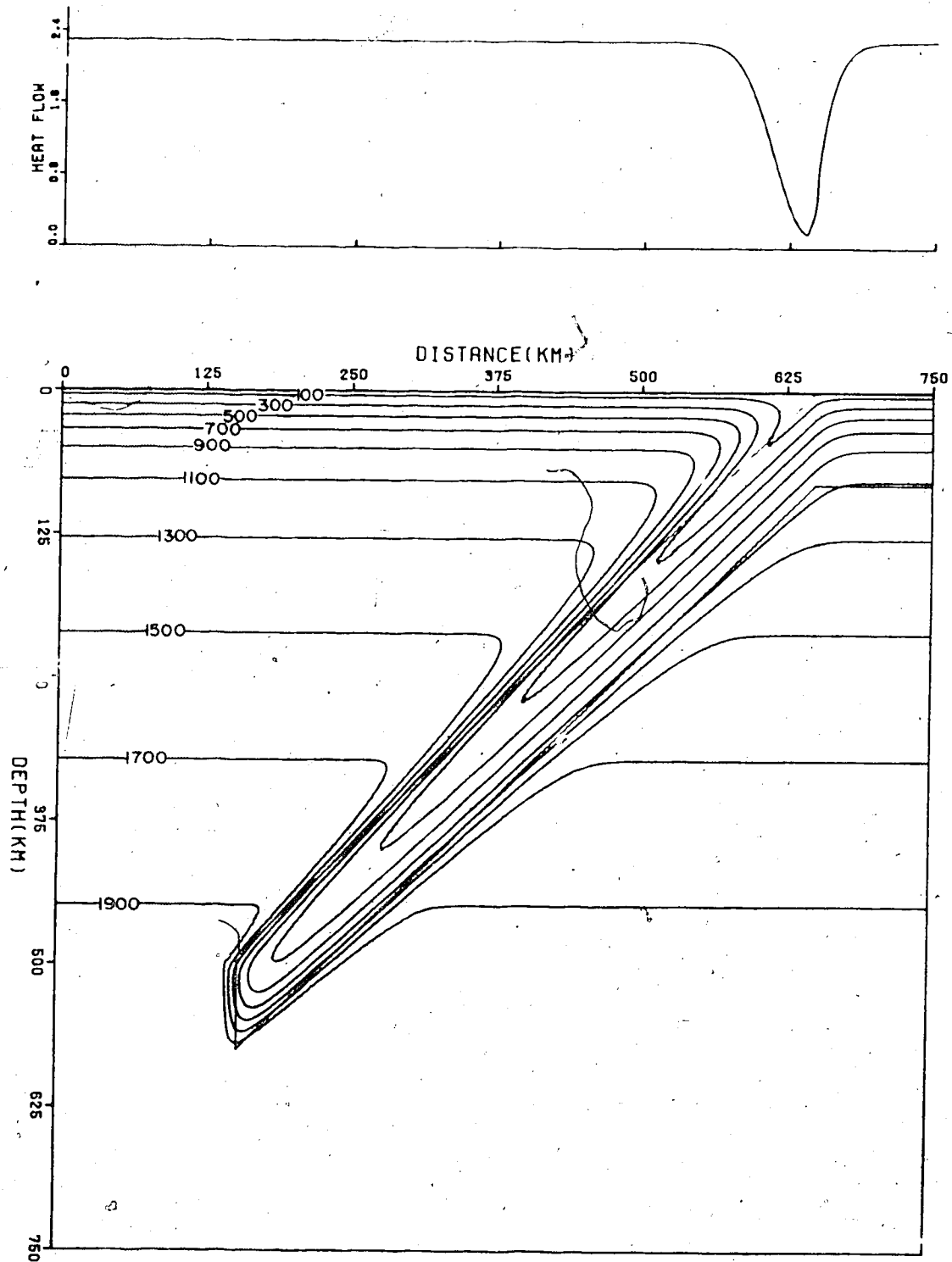


Fig. 16. The temperature regime and surface heat flow profile for a  $45^\circ$  dipping slab with a velocity of 8.0 cm/year. Heat transport is by conduction only.

conduction is considered as the only process which governs the slab's thermodynamics. Figure 16 shows the associated temperature field and surface heat flow profile for the descending slab. From the figure it is seen that the slab remains cooler than the surrounding mantle to depths greater than 500 km indicating that heat conduction alone is insufficient to allow slab assimilation into the upper mantle. The increased slab velocity as compared with that of Figs. 3-5 results in the heat flow profile dipping to near zero values at the point of subduction. This suggests slab dynamics may be indicated by the magnitude of heat flow observations in ocean trenches. Lower heat flow values in one trench relative to another may indicate that the velocity of the slab with lower heat flow may be greater than the slab which displays higher heat flow in the trench region. It is uncertain whether this effect will be masked by regional anomalies of a near surface origin.

The effects of adiabatic compression and shear-strain heating on a 45° dipping slab with a subduction velocity of 8.0 cm/year are shown in Fig. 17. Shear heating occurs in the same areas as mentioned with regard to Fig. 11 and has a magnitude of  $6.0 \times 10^{-4}$  ergs/cm<sup>3</sup>-sec along the top surface of the slab and an order of magnitude lower term along the bottom surface of the slab. The implied viscosity in the shear zone along the top surface of the slab is approximately  $10^{22}$  poise. The combined effect of adiabatic compression and shear heating is to warm the interior of the

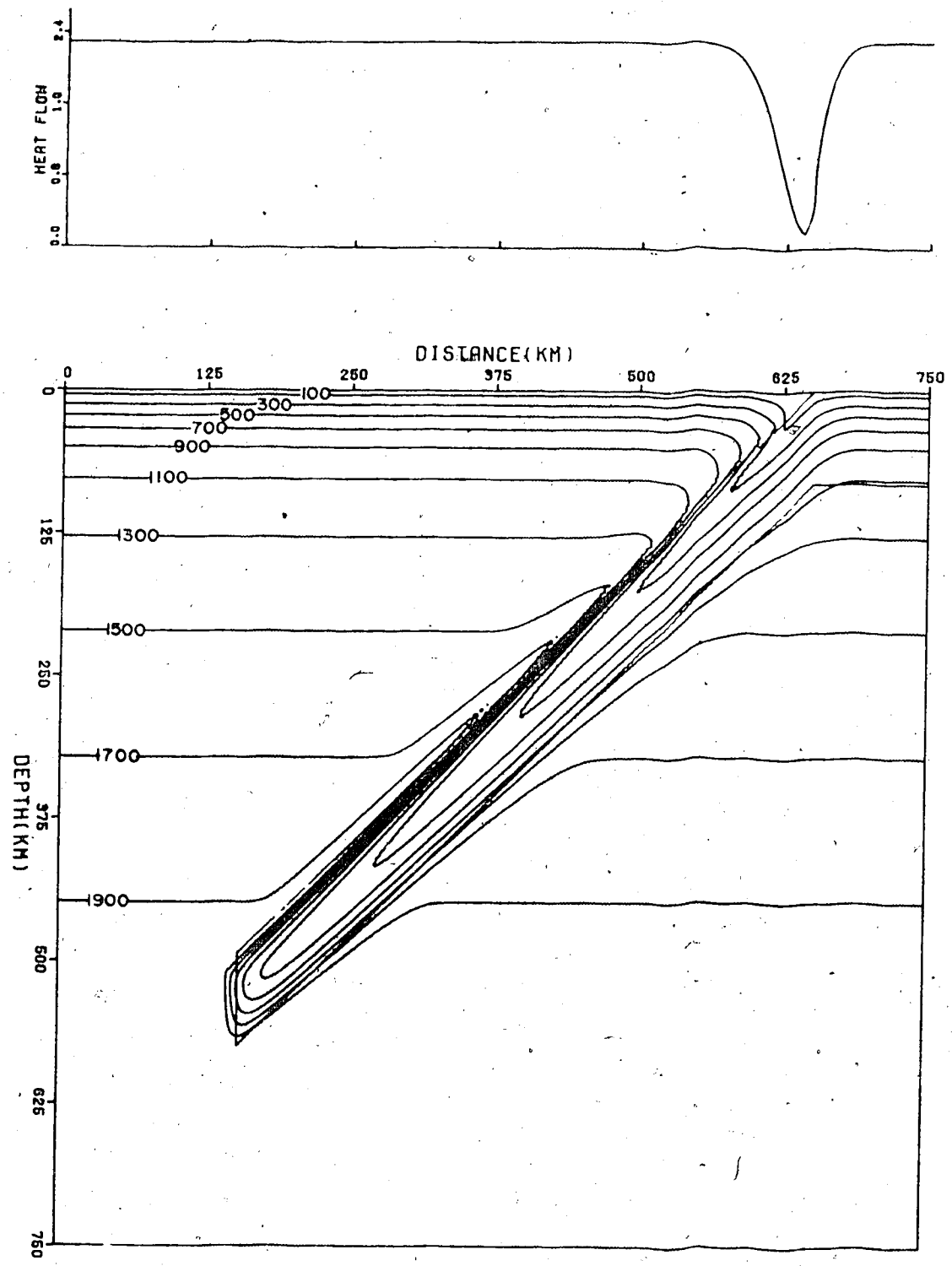


Fig. 17. As Fig. 16, but with adiabatic compression and shear heating included as heat sources.

slab substantially as compared with heat conduction alone. Shear heating along the upper surface of the slab raises the temperatures above the basalt solidus (Fig. 18, curve C) in depths ranging from 175 km to 350 km (Fig. 18, curve A). The effect of shear heating is not observed at the earth's surface due to the periods of time considered. Figure 18 (curve B) gives the temperature-depth profile (along the upper surface of the slab) for a slab dipping at  $26.6^\circ$ . The shear zone thickness for the  $26.6^\circ$  slab is slightly larger than that for the  $45^\circ$  dipping slab in the direction of subduction, resulting in more intense heating along the shallower slab. This increased shear zone thickness is a result of the descent mechanism as described previously (Sec. 3.3.a). The vertical velocity of the  $26.6^\circ$  dipping slab is 5.6 cm/year, resulting in a subduction velocity of 12.5 cm/year. The effect of a much larger subduction velocity is negated by shear heating along the slab's upper surface since it is expected a greater subduction velocity will tend to maintain cooler temperatures along the slab's upper surface. The region of partial melting is extended from 100 km to approximately 400 km depth in the  $26.6^\circ$  case (Fig. 18, curve B).

The effect of increased shear-strain heating in the  $26.6^\circ$  and  $45^\circ$  dipping slabs is illustrated in Fig. 19. Figure 19 (curve A) gives the temperature-depth profile along the upper surface of a  $45^\circ$  dipping slab with shear heating along this upper surface amounting to  $7.0 \times 10^{-4}$



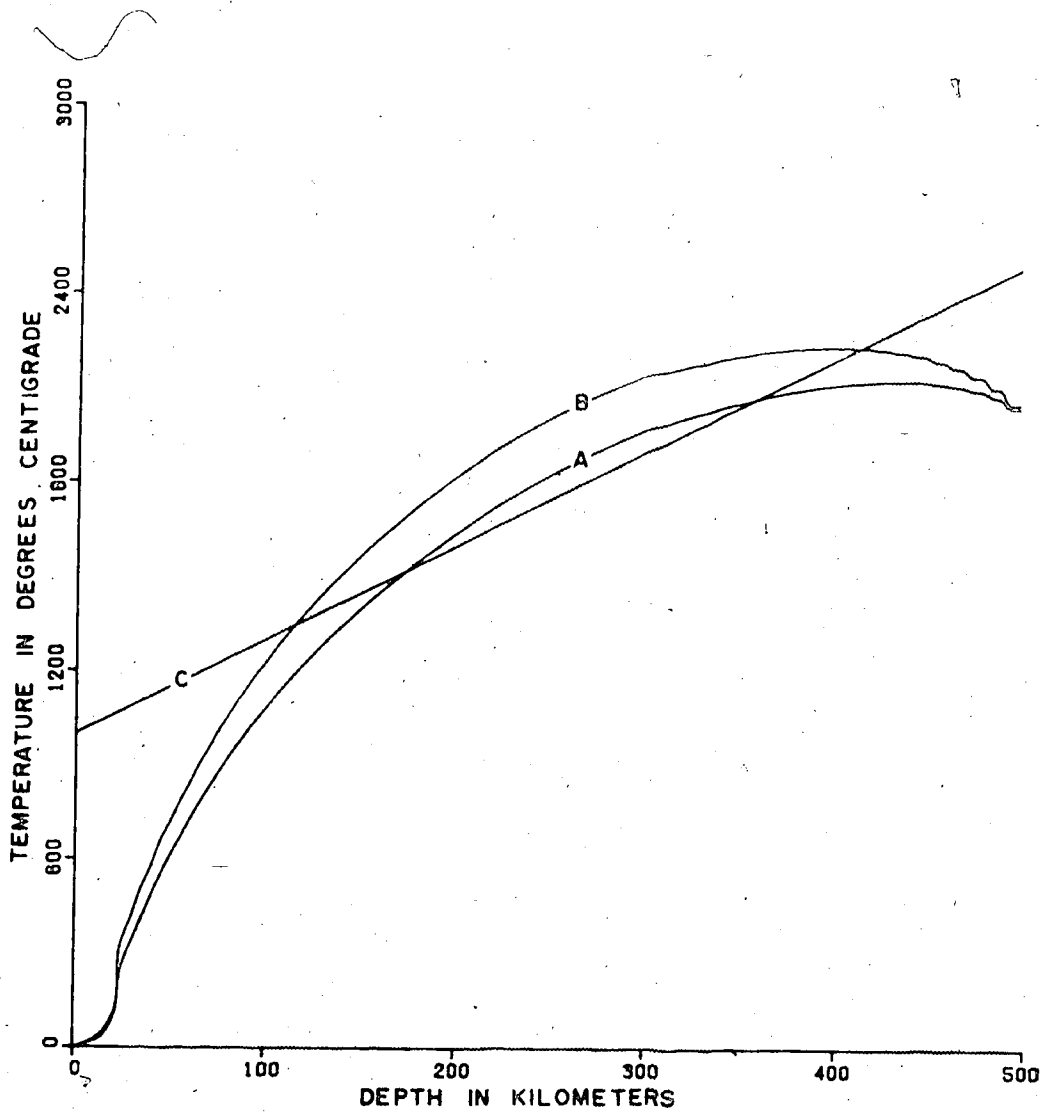


Fig. 18. Temperature-depth profiles along the upper surface of the slab for Fig. 17 (curve A) and for a slab slipping at  $26.6^\circ$  with the same heat sources as in Fig. 17 (curve B).

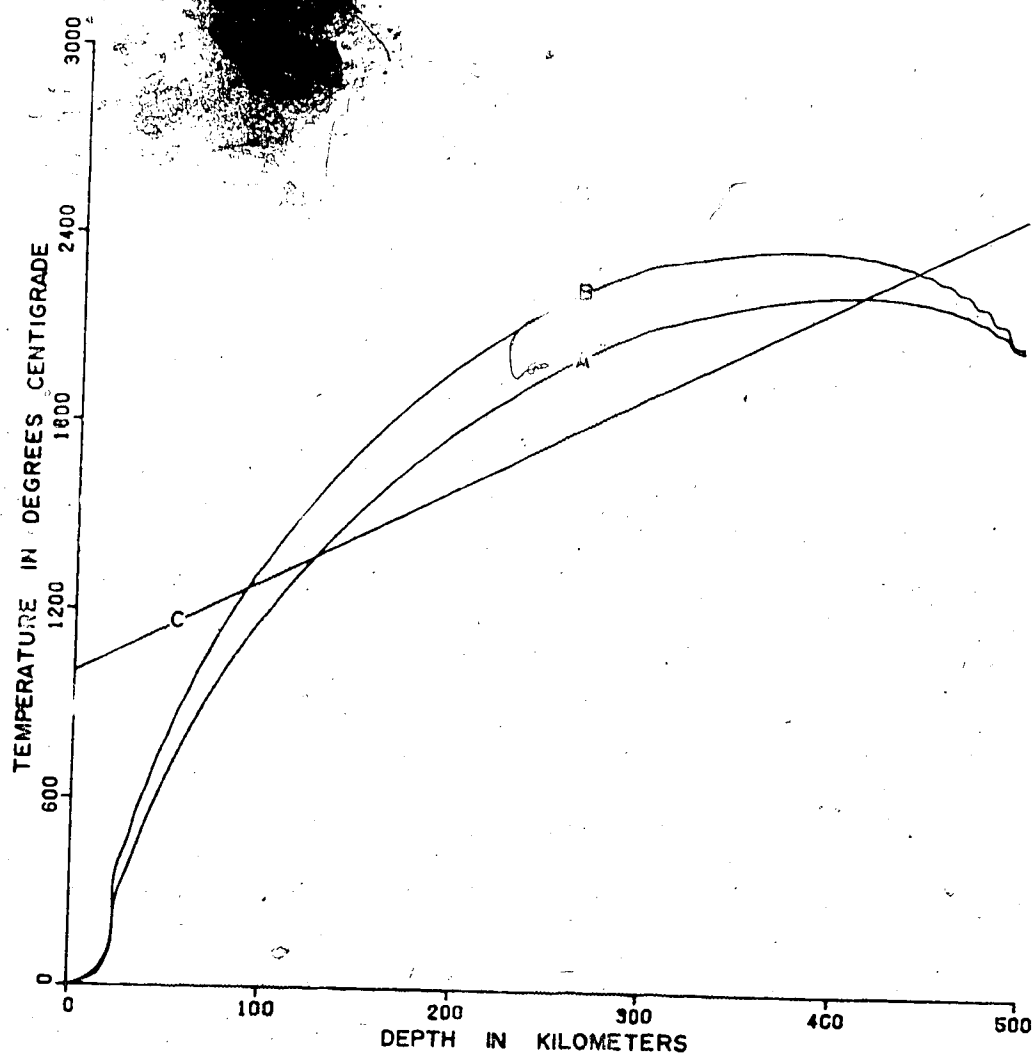


Fig. 19. As Fig. 18, but with shear heating increased by 15% for a  $45^\circ$  dipping slab (curve A) and a  $26.6^\circ$  dipping slab (curve B). Curve C is the basalt solidus.

ergs/cm<sup>3</sup>-sec. The corresponding 15% increase in shear heating along the upper surface extends the region of partial melting from 100 km to 400 km depth, an increase of 70%. A similar increase is noted for the 26.6° case as shown in Fig. 19 (curve B). The shear zone has a shear heating coefficient of  $7.0 \times 10^{-4}$  ergs/cm<sup>3</sup>-sec and is 10 km in vertical thickness along the upper surface of the slab. The thickness of the region of partial melting is increased by 20%. The above results indicate that a small increase in the shear heating along the upper surface of the slab produces large changes in the thermal fields of the respective slabs. Shear heating may control the regions of partial melting in the descending slab while being directly controlled itself by the amount of stress propagated by the coupling of the slab-mantle interface.

#### 3.4 Gravity Effects of the Downgoing Slab

Figures 20-21 indicate gravity effects due to sinking slabs with various heat sources and rising material from the upper surface of the slab. Figure 20 illustrates the gravity effect for slabs dipping at 45°. In Fig. 20, curve A gives the results for a slab with a vertical velocity of subduction of 0.7 cm/year and adiabatic compression included with shear heating along the upper surface of the slab (as in Fig. 11). The resulting gravity effect indicates a weak negative anomaly over the horizontal axis. The effect of the cold sinking slab is masked by the partial melt created at

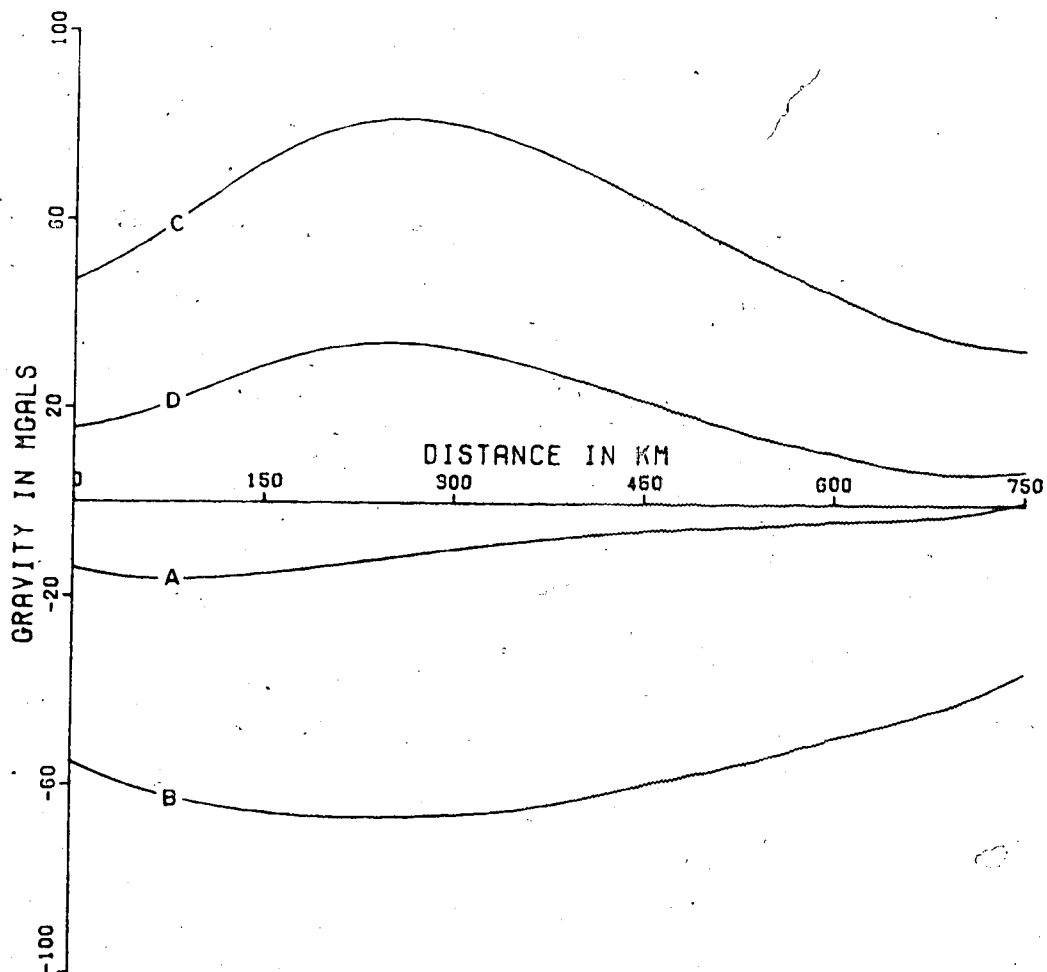


Fig. 20. Gravity profiles across the horizontal extent of subduction for a  $45^{\circ}$  dipping slab. Curves A, B, C and D correspond to the models of Figs. 11, 14, 16 and 17 respectively.

the upper surface of the slab. Figure 20 (curve B) represents the gravity effect due to a  $45^\circ$  dipping slab with partial melt rising from the slab's upper surface (as in Fig. 14). The resulting gravity anomaly shows a broad regional low with a trough of approximately 60 milligals. The effect of the rising melt again masks the dynamics of the cold descending lithosphere. The anomaly has a long wavelength which results from the horizontal extent over which rising melt occurs. Figure 20 (curve C) illustrates the effect of a  $45^\circ$  dipping slab with subduction velocity of 8.0 cm/year (as in Fig. 16). The effect of a cold sinking slab warmed only by heat conduction is represented by a positive regional anomaly with a peak of approximately 75 milligals. The large positive anomaly results from the large subduction velocity causing the lithosphere to remain cooler than the surrounding mantle to depth of 500 km. In Fig. 20, curve D is the gravity effect of an 8.0 cm/year subducting slab warmed by adiabatic compression and shear heating (as in Fig. 17). The additional heat sources cause the peak of the anomaly to be lowered to about 25 milligals as a result of less dense material being formed along the upper surface of the slab.

Marine gravity data produced by Hayes (1966) indicates that there is a small positive anomaly of approximately 20-30 milligals extending 200-500 km toward the continental side of subduction across the Chile trench at  $23^\circ\text{S}$ . This anomaly is consistent with Fig. 20 (curve D) for a slab

subducting at 8.0 cm/year. The subduction velocity and angle of descent are consistent with data available on the Chile trench (Le Pichon et al, 1973) which indicates the lithosphere plate velocity to be about 6.0 cm/year. The observed negative anomaly of approximately -200 milligals, in the Chile trench, is due to low-density ocean-floor sediments near the trench axis (Grow and Bowin, 1975). Watts and Talwani (1973) calculated the gravity effects in subduction zones and concluded that the gravity effect of the downgoing slab is confined to the island arc and trench region, which is consistent with gravity profiles calculated here. The gravity profiles considered allow some investigation into the study of slab dynamics. A broad regional negative anomaly (Fig. 20 curve B) may indicate that a substantial amount of partial melt has risen from the top of the slab creating a low density region over the continental side of subduction. The anomaly can also indicate that the slab is moving with a relatively small velocity (approximately 1.0 cm/year) preventing large temperature gradients from occurring (allowing the slab to warm to mantle temperatures). Alternatively, a large positive anomaly may indicate a slab moving at greater subduction velocities (approximately 8.0 cm/year) not having enough time to warm to mantle temperatures.

Figure 21 gives results for different slabs dipping at  $26.6^\circ$  with various heat sources. Figure 21 (curve A) shows the gravity effect due to a slab with shear heating and

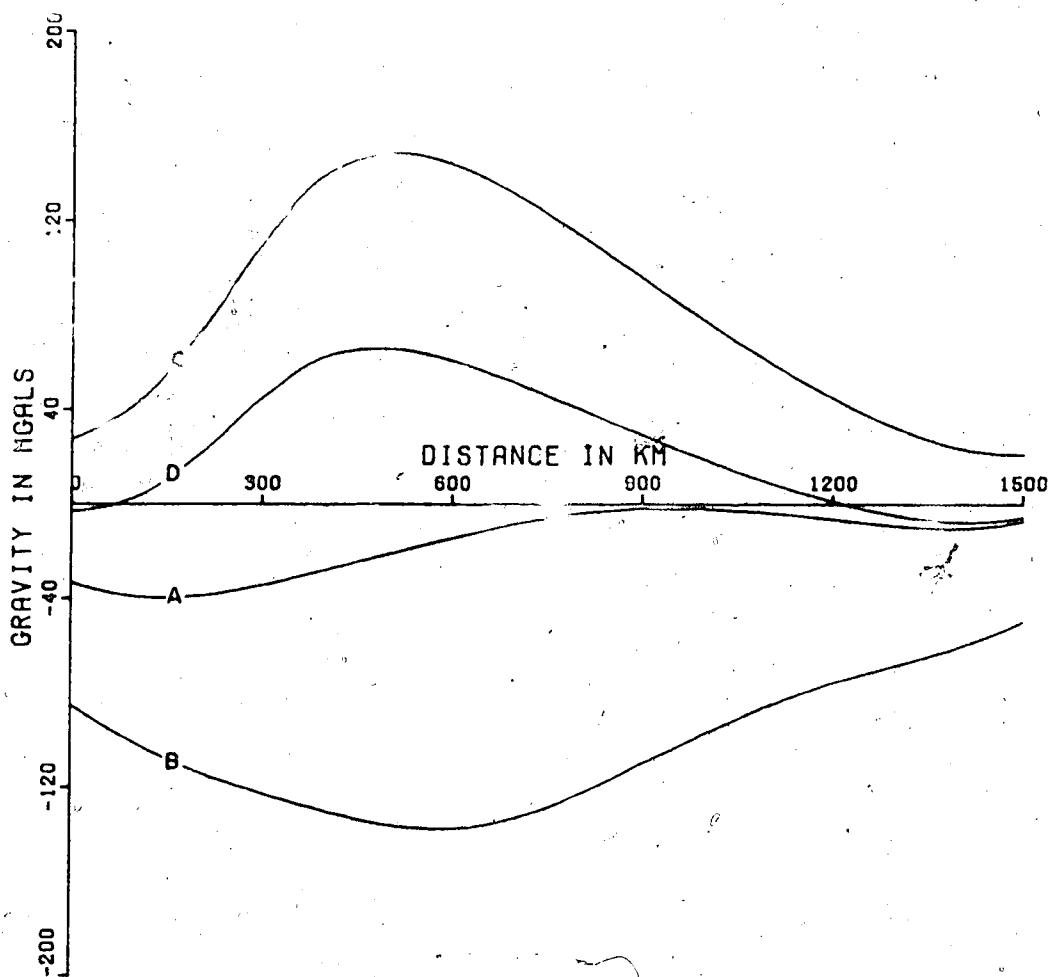


Fig. 21. Gravity profiles across the horizontal extent of subduction for a  $26.6^\circ$  dipping slab. Curves A and B correspond to the models of Figs. 13 and 15 respectively. Curve C is associated with a slab descending at 12.5 cm/year with only heat conduction considered. Curve D is associated with a slab descending with the same velocity but with adiabatic compression and shear heating added.

adiabatic compression having a vertical velocity of 0.7 cm/year (as in Fig. 13). The resulting anomaly is negative over the trench region, moving to near zero 400 km to the left of subduction (as in the figure) and falling to -40 milligals about 1000 km from the point of subduction on the continent side. Figure 20 (curve B) represents the gravity effect of a slab moving with a vertical velocity of 0.7 cm/year with rising melt (as in Fig. 15). There is a large negative anomaly with a trough of -140 milligals due to the low density rising material. The effect of the cold sinking slab is masked by the rising melt except for a short wavelength anomaly at the 1000 km point along the horizontal axis. Figure 21 (curve C) is the gravity effect due to a slab dipping at  $26.6^\circ$ , moving with a vertical velocity of 5.0 cm/year with only heat conduction considered. Figure 21 (curve D) is similar to Fig. 21 (curve C) except for adiabatic compression and shear heating considered as heat sources. The resulting positive anomaly peaking at 150 milligals in Fig. 21 (curve C) is lowered by the shear heating and adiabatic compression as shown in Fig. 21 (curve D).

Comparison of Figs. 20 and 21 indicates that the gravity anomalies for the shallower dipping slab are of much larger amplitude and extend over a larger region. This is due to the descent mechanism which causes the shallower dipping slab to maintain a greater thickness and therefore a larger region of density anomaly. The implications for slab



dynamics are that a shallower dipping slab (i.e.  $26.6^\circ$ ) which has penetrated into the mantle to the same depth as a steeper dipping slab (i.e.  $45^\circ$ ) will display a larger gravity anomaly due to the descent mechanism involved in subduction as well as the velocity of subduction over the same time periods considered. The descent mechanism causes a slab dipping at a shallower angle (i.e.  $26.6^\circ$ ) to maintain a greater thickness in the direction of subduction as well as being subducted over a greater horizontal region to reach the same depths as a steeper dipping slab (i.e.  $45^\circ$ ). The result is more slab material being subducted in the shallower dipping slab adding to the gravity anomaly. The greater subduction velocity in the shallower dipping slab causes the isotherm to be pulled further into the mantle creating a larger positive anomaly than a steeper dipping slab, over the same time period.

### 3.5 Summary of Results

The results presented in this chapter describe the thermal and gravity effects of a downgoing slab heated by conduction, adiabatic compression and viscous dissipation. From the results, the effect of dip angle on the thermal regime is to maintain lower temperatures with the slab at gentler dips (i.e.  $26.6^\circ$ ) over the same time period and depth interval considered as compared with a steeper dipping slab (i.e.  $45^\circ$ ). This result may be explained by the greater subduction velocity needed to reach the same depths in the

same time periods considered as well as the greater slab thickness requiring more energy to be heated to surrounding mantle temperatures in the gentler sloping slab. This effect is largely negated along the upper surface of the slab when shear heating is considered. Shear heating raises the isotherms locally to a greater extent in the gentler sloping slab due to the larger region over which this heating occurs. The descent of the slab causes a dip in the heat flow near the point where subduction begins resulting from the inability of the slab to reach thermal equilibrium with surrounding material at shallow depths. The various heat sources within the slab do not affect the heat flow at the surface in the time periods considered.

The subduction velocity affects the temperature field within and around the descending slab. A large subduction velocity (i.e. 8.0 cm/year) causes the temperatures within the slab to remain much lower than the surrounding mantle as compared with a low subduction velocity (i.e. 1.0 cm/year). This effect, in turn, requires a greater amount of shear heating in the faster moving slab to create partial melt along the upper surface of the slab. The faster moving slab creates a lower minimum in the heat flow profile near the point where subduction begins as compared to a slower moving slab.

Rising melt, generated at depth, creates a high in the heat flow pattern over the horizontal extent to which this melt occurs. The region of rising melt is larger in the

shallower dipping slab (i.e.  $26.6^\circ$ ) creating a heat flow high over a wider region than the steeper dipping case due to the depth range over which the melt is forced to rise (the same in both cases). Large horizontal temperature gradients occur at the vertical boundaries of the rising melt.

The density variations within the subduction zone resulting from the perturbed thermal regime create anomalous gravity effects at the earth's surface. The cold sinking slab creates a broad positive anomaly over the horizontal extent of subduction resulting from the slab being denser than the surrounding medium. The gravity effect of the sinking slab is masked by the creation of partial melt at the surface of the slab which rises creating a negative anomaly over the region of interest. The effect is more pronounced over the shallower sloping slab (i.e.  $26.6^\circ$ ) because of the larger region over which partial melt occurs as compared with the steeper dipping case (i.e.  $45^\circ$ ). These gravity effects may be altered by the presence of density anomalies in the crust as well as topography variations.

The variations in heat flow and gravity within a subduction zone presented in this chapter have implications in the study of slab dynamics. By studying the changes in the observables, it may be possible to obtain a better understanding of processes occurring within subduction zones and quantitative estimates of the magnitudes of these processes. An attempt has been made to determine changes in

heat flow and gravity as a result of a slab descending into the mantle under various conditions. It is hoped that the results obtained may be applied to the further study of slab dynamics in regard to heat flow and gravity in subduction zones and related island arc regions.

CHAPTER 4 THE EFFECT OF SUBSURFACE TEMPERATURE  
VARIATIONS ON THE BEHAVIOUR OF TIME-VARYING  
ELECTROMAGNETIC FIELDS

4.1 Description of the Models

The electrical conductivity of the earth is in general a complicated function of several variables including temperature and pressure. The effect of pressure on conductivity is not well known although some work has been done on the variation of conductivity with pressure-induced phase transitions at depths between 400 km and 900 km (Rikitake, 1959, Akinoto and Fujisawa, 1965). Although the present numerical analysis includes regions at depths of 600 km, the variation in conductivity as a function of pressure is ignored. The relationship between temperature and electrical conductivity can be expressed as:

$$\sigma = \sigma_1' e^{-E_1/2kT} + \sigma_2' e^{-E_2/2kT} + \sigma_3' e^{-E_3/kT} \quad (14)$$

taking into consideration three different conduction mechanisms; impurity, intrinsic, and ionic (Rikitake, 1966). In the above equation,  $(\sigma')_{1,2,3}$  denote the conductivities at infinite temperature,  $(E)_{1,2,3}$  denote the excitation energies,  $T$  is the absolute temperature and  $k$  is the Boltzmann constant. The temperature dependence of the excitation energy is contained in the values for  $(E)_1$ . This dependence occurs because of the dominance of different

conduction terms in specific temperature intervals. Although the excitation energy is expected to depend upon pressure, only crude estimates have been obtained as to an exact relationship (Rikitake, 1966) and therefore the effect has been ignored in the present models. Since the composition of the mantle consists mostly of olivine-pyroxene minerals, it is reasonable to choose the following values for the constants:  $\sigma_1^0 = 10^{-14}$ ,  $\sigma_2^0 = 10^{-9}$ ,  $\sigma_3^0 = 10^{-6}$ ,  $E_1=1$ ,  $E_2=E_3=3$ , where  $\sigma^0$  is in emu and  $E$  is in electron volts (Rikitake, 1966). The conductivity distribution does not take into consideration specific variations related to melted material other than those due to temperature.

The thermal models considered in this work are:

Model (a): This model gives the temperature distribution corresponding to the time when the slab just begins to descend (Initial state),

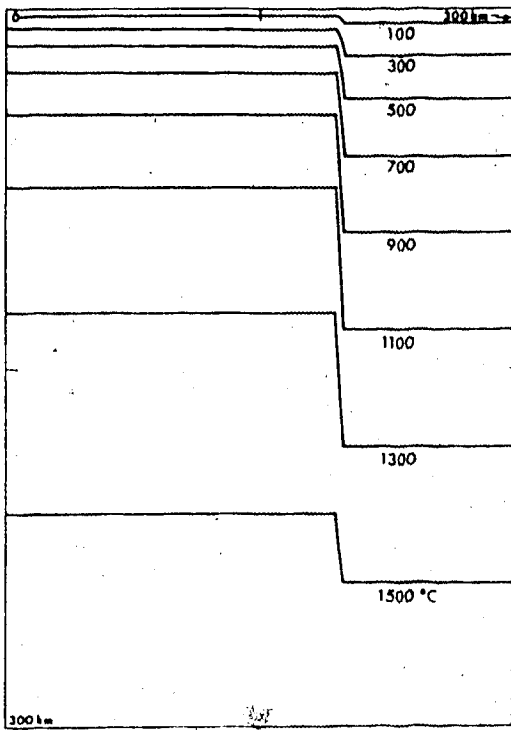
Model (b): This gives the temperature distribution after the slab has descended for a period of 21.2 million years with heat conduction considered as the only mechanism of heat transport (Final state),

Model (c): The period of subduction is the same as that of model (b), but the temperature distribution is influenced by partial melting along the upper surface of the slab,

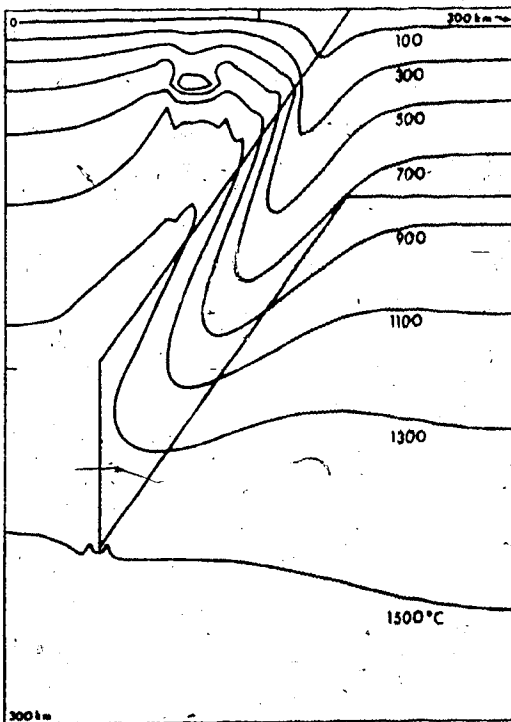
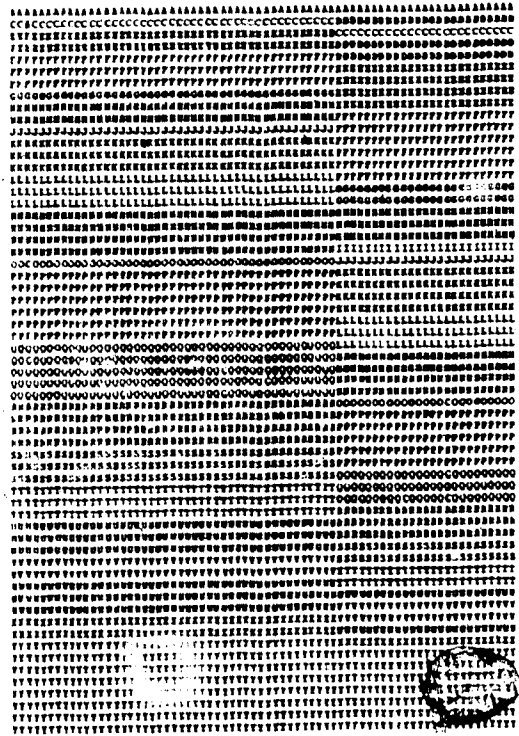
Model (d): The period of subduction is the same as that of model (b), but this model assumes that the material melted along the surface of the slab rises to within 30 km of the earth's surface. In models (b), (c), and (d) the angle of subduction of the slab is  $45^\circ$  and its downgoing velocity is 1.0 cm/year. The vertical thickness of the slab is taken to be 80 km.

Figure 22 shows the temperature distribution obtained for model (a) (Fig. 22a - left) and for model (d) (Fig. 22b - left). The temperature distributions for models (b) and (c) are not shown. The dimensions of each model are 300 km x 300 km. The temperature varies from  $0^\circ\text{C}$  at the surface to approximately  $1700^\circ\text{C}$  at a depth of 300 km. The electrical conductivity model shown in Fig. 22a (right) corresponds to the thermal model (a), and that shown in Fig. 22b (right) corresponds to model (d). Since the finite-difference numerical method for the electromagnetic calculations requires that the conductivity distribution be divided into various cells, each with a specified conductivity value, small variations in temperature (and conductivity) are ignored. The values assigned to each conducting cell are shown in Fig. 22.

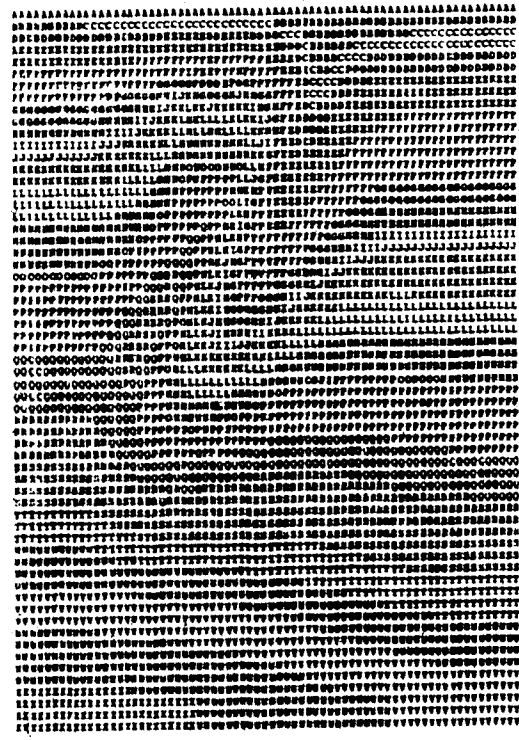
Figure 23 shows the geophysical model considered in this work. It consists of a conducting layer of thickness 'd' and of two different conductivities  $\sigma_1$  and  $\sigma_2$  overlying the conductivity distribution determined by each of the four thermal models. The inducing source field is assumed to be



(a)



(b)



A = 1.02-23	F = 1.07-16	E = 2.36-15	P = 2.28-16	G = 7.02-16
B = 1.02-20	G = 2.51-16	L = 5.02-15	O = 3.02-16	H = 6.02-16
C = 1.02-17	H = 2.17-16	M = 7.02-15	Q = 4.02-16	I = 7.02-16
D = 1.02-16	I = 2.51-16	N = 4.02-15	R = 5.02-16	J = 1.02-13
	J = 1.02-15	U = 6.02-16	T = 6.02-16	K = 2.02-13

Fig. 22. Temperature distribution and electrical conductivity models for (a) the initial state, and (b) the final state. The conductivity values are in emu units.



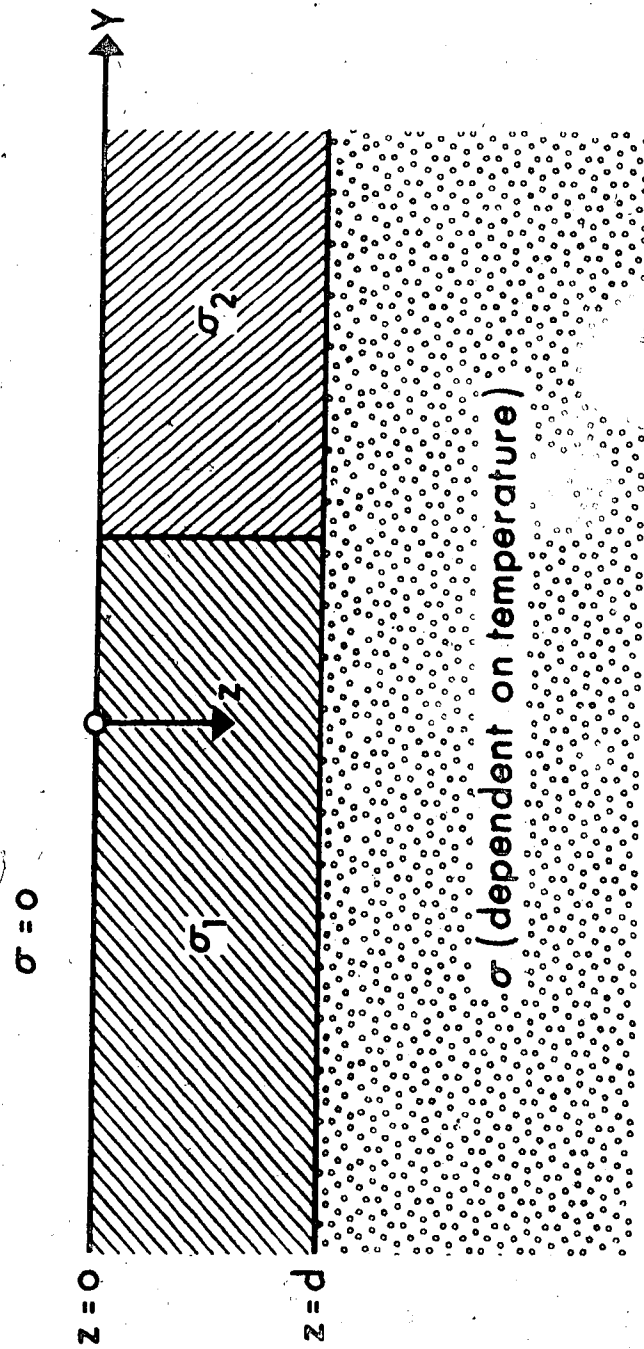


Fig. 23. The geophysical model.

uniform with its horizontal electric component in the x-direction (E-polarization). The frequency of oscillation is chosen to be 0.75 Hz.

The electromagnetic modelling technique used in the present work is basically the same as that described by Jones and Pascoe (1971) and Pascoe and Jones (1972), with the modifications proposed by Williamson et al. (1974) and Brewett-Taylor and Weaver (1976). The technique is based on the finite-difference approach to the solution of Maxwell's equations in two dimensions and has been extensively used in investigating various conductivity anomalies (Jones, 1973). In the numerical method a 71 x 71 grid of mesh points with variable grid dimensions is superimposed on the geophysical model shown in Fig. 23. It is noted that, for large positive and negative values of  $\gamma$ , the conductivity models of Figs. 22 and 23 have layered structure, which is one of the boundary conditions to be satisfied in the numerical method of Pascoe and Jones (1972). It should be mentioned here that for the convenience of display only a part of the 71 x 71 grid used is shown in Fig. 22. The lower boundary in the electromagnetic numerical model has been chosen at  $z = 130$  km, whereas the lower boundary in the heat flow numerical model is at  $z = 300$  km. This difference in the depths of the lower boundary implies that it has been assumed the temperature is constant between depths of 300 km and 630 km. This assumption permits the lower boundary in the electrical conductivity configuration to be far away from the earth-air

interface  $z = 0$ .

#### 4.2 Discussion of Results

The numerical calculations for the electric and magnetic field components have been carried out for two different cases: (1) the conductivity of the lower layer is varied while the conductivities of the upper layer,  $\sigma_1$  and  $\sigma_2$ , and its thickness are kept constant, and (2) the conductivity  $\sigma_2$  is varied while keeping  $d$ ,  $\sigma_1$  and the conductivity of the lower layer constant. In the following discussion,  $E_x$  denotes the amplitude of the horizontal electric field component, whereas  $H_y$  and  $H_z$  denote the amplitudes of the horizontal and vertical magnetic components, respectively. The apparent resistivity is defined as  $\rho_a = (0.2/f) (E_x/H_y)^2$ , where  $f$  is the frequency in hertz,  $E_x$  is in mV/km,  $H_y$  is in oersteds and  $\rho_a$  is in emu. The surface heat flow is expressed in units of microcalories/(cm<sup>2</sup>-sec). To distinguish between the electromagnetic models and the heat flow models, letters A, B, C and D refer to the electromagnetic models (Fig. 23) in which the lower layer configuration is determined by the conductivity distribution corresponding to the heat flow models a, b, c or d, respectively.

To study the effect of the subsurface temperature variations on the electric and magnetic fields observed at the earth's surface, calculations were carried out for models A, B, C and D by choosing  $d = 5$  km for the upper layer

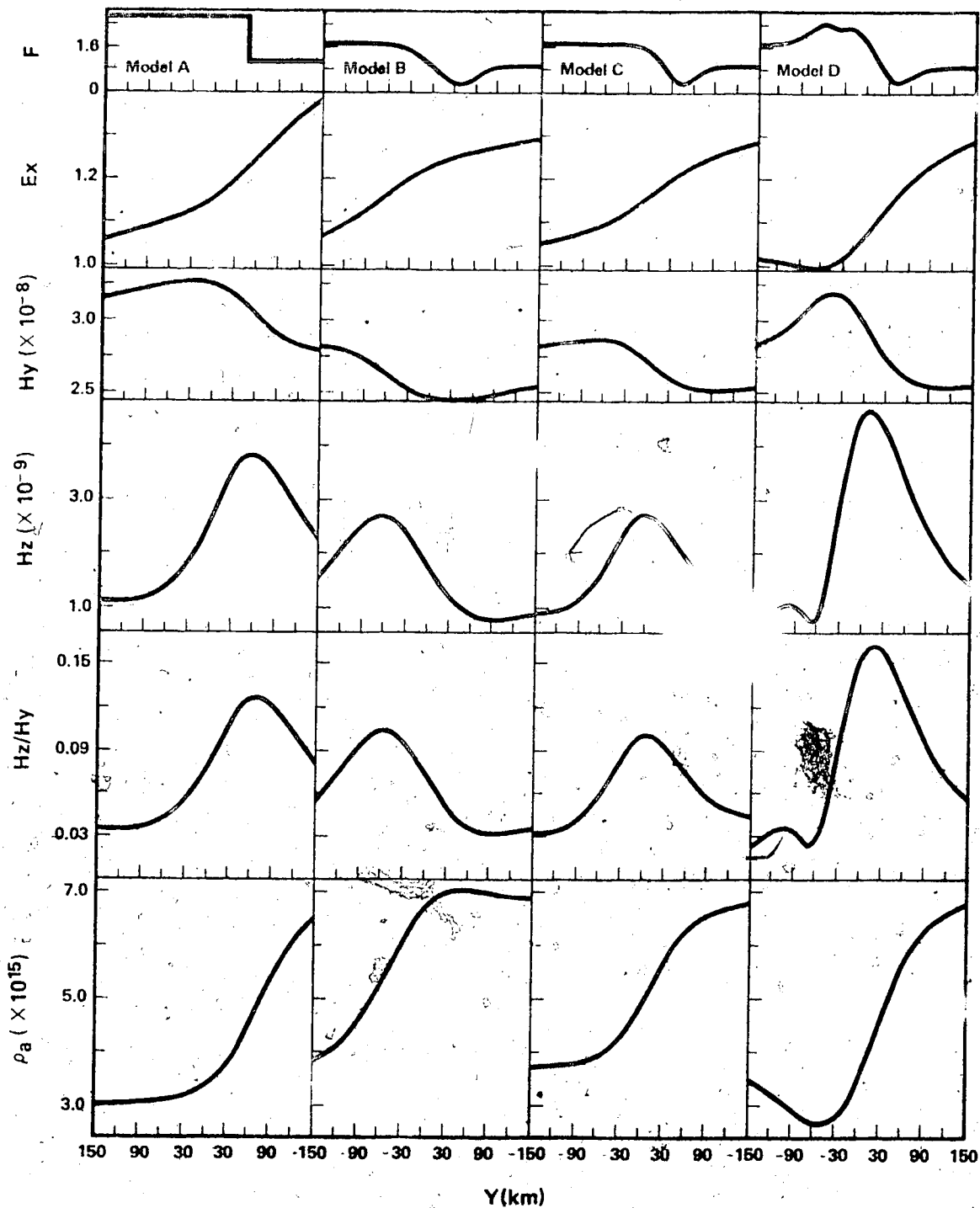


Fig. 24. The spatial variation of heat flow and the electromagnetic field components at the surface  $z=0$  for different conductivity models, with  $d=5$  km and  $\sigma_1=\sigma_2=10^{-15}$  emu.

depth and  $\sigma_1 = \sigma_2 = 10^{-15}$  emu for the upper conductivities. Figure 24 shows the spatial behaviour of the amplitudes  $E_x$ ,  $H_y$ ,  $H_z$  and their ratios for points at the surface  $z = 0$  along the  $y$ -direction (i.e. perpendicular to the source electric field). Although the results are presented only for the region  $-150 \text{ km} \leq y \leq 150 \text{ km}$ , the left and right outer boundaries of the numerical calculations for the conductivity models are kept far beyond  $y = \pm 150 \text{ km}$ . This is done in order to satisfy the boundary conditions which require that in regions far away from the anomaly, the conductivity structure is layered and that the fields there remain unperturbed. The factors that appear on the ordinates of some of the amplitude curves are the scaling factors which are to be used in determining the exact amplitude. For example, at  $y = -150 \text{ km}$ , the apparent resistivity for model A has the value of approximately  $1.0 \times 10^{15}$  emu's.

It is evident from the results shown in Fig. 24 that the surface heat flow  $F$  for the final state (models B-D) is less than that for the initial state (model A). This is mainly due to cooling in the mantle since the beginning of subduction. As the high temperature isotherms rise to the surface (models C and D)  $F$  shows a general enhancement. The heat flow  $F$ , which undergoes an abrupt change near  $y = 40 \text{ km}$  for the initial state, exhibits a smooth variation for the final state, with a slight horizontal shift of about  $5 \text{ km}$  in the location of its minimum. The 'kink' that appears in  $F$  for the model D shows the effect of rising hot material from

the upper surface of the descending slab. Since the results for the electromagnetic field components shown in Fig. 24 correspond to the electromagnetic model with uniform source field and a uniformly conducting overburden, any variation in the spatial behaviour of the field components can be attributed to the subsurface temperature variations. The results for the horizontal electric component indicate that  $E_x$  in general has low amplitude in the regions where there is increased heat flow and high amplitude in the regions with decreased heat flow. Noting that the only difference between models B and C is that the latter assumes the presence of melted material along the slab, it is readily observed that these materials which are responsible for the increased heat flow cause a reduction in the  $E_x$  amplitudes observed at the surface. The rising of hot material from the slab (model D) considerably affects both the amplitude and shape of the  $E_x$  component.

As expected, the horizontal magnetic component  $H_y$  has large amplitude in regions of increased heat flow. In the case of the initial temperature distribution (model A),  $H_y$  increases gradually as the region where  $F$  undergoes a sudden variation (near  $y = 40$  km) is approached, reaching a maximum near  $y = -10$  km over the higher heat flow side. Beyond this point,  $H_y$  falls off and gradually approaches a constant value for large values of  $|y|$  as required by the uniform source field. For model B however,  $H_y$  does not exhibit any pronounced maximum but instead undergoes a minimum

approximately where the surface heat flow is a minimum. As the high temperature isotherms rise to the surface (models C and D)  $H_y$  again shows behaviour similar to that of  $H_y$  for model A.

The behaviour of the vertical magnetic component ( $H_z$ ) at the surface appears to be more sensitive to the subsurface temperature variations than the behaviour of the horizontal component ( $H_y$ ). This is particularly evident in the horizontal shift in the location of the peak value of  $H_z$  which is considerably affected by the rate of decrease (as a function of  $y$ ) of the surface heat flow. A comparison of the behaviour of  $H_z$  with that of  $H_y$  indicates that with respect to the location where  $F$  undergoes a rapid variation, the maximum amplitude for  $H_y$  always occurs over the higher heat flow regions whereas the maximum of  $H_z$  occurs some distance to the right over the decreased heat flow side. The results also indicate that the movement of hot magma from the slab (model D) has considerable influence on the amplitude as well as on the general behaviour of the vertical component.

The results for the vertical to horizontal magnetic field ratio ( $H_z/H_y$ ) and the apparent resistivity ( $\rho_a$ ) are also given in Fig. 24. The behaviour of  $H_z/H_y$  as a function of  $y$  is very similar to that of  $H_z$ . The apparent resistivity is, as expected, less over the higher heat flow regions than over the lower heat flow regions. Like the other field components,  $\rho_a$  is also influenced by the subsurface temperature variations, the most noticeable effects being

7

due to the melted material that has risen from the slab.

Figure 25 shows the contours of equal amplitude of the subsurface temperature distribution and of the three field components for models A-D. Only the temperature distribution below the surface  $z=0$  is shown, since it has been assumed that in the numerical model for the heat flow problem, the temperatures for  $z \leq 0$  remain unperturbed and are taken to be zero for convenience. For the electromagnetic fields, the amplitude contours include both the free-space region ( $z \leq 0$ ) and the conducting region ( $z > 0$ ). It must be noted that the contour values of each of the three components are the same for the four models. One feature that is readily apparent is that the effect of the subsurface temperature variations is more pronounced in the amplitude contours of  $H_y$  and  $H_z$  than in the contours of  $E_x$ . The contours for the vertical component for the four models show clearly the horizontal shift in the location of the  $H_z$  maxima that was observed earlier (Fig. 24). The presence of the two maxima in  $H_z$  is also evident in the contour plots for model D.

The effect on the electromagnetic fields of varying the upper layer conductivity contrast has been studied by varying the conductivity  $\sigma_2$  while keeping both  $\sigma_1$  and  $d$  constant. Figure 26 gives the results from  $H_z/H_y$  and  $\rho_a$  at the surface for various values of  $\sigma_2/\sigma_1$  for model D with  $d = 2$  km and  $\sigma_1 = 10^{-15}$  emu. At the frequency of 0.75 Hz, the skin depths in the conductivity  $\sigma_2$  are 58, 18, 5.8, and 1.8 km for  $\sigma_2/\sigma_1 = 1, 10, 10^2, \text{ and } 10^3$ , respectively. The



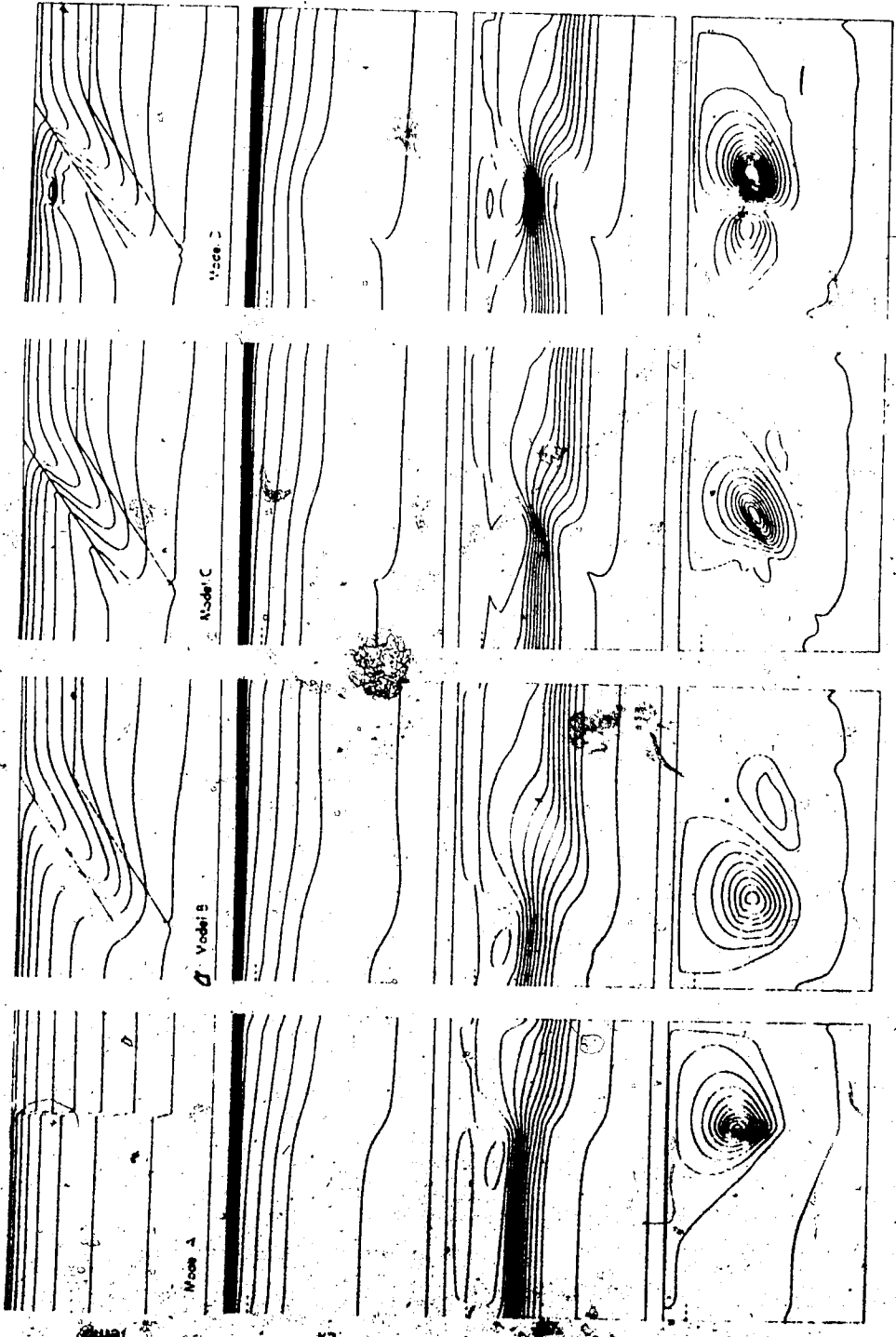


Fig. 25. Contours of equal amplitude of temperature and electromagnetic fields for different conductivity models. (The horizontal dashed line indicates the location of the surface  $z=0$ .)

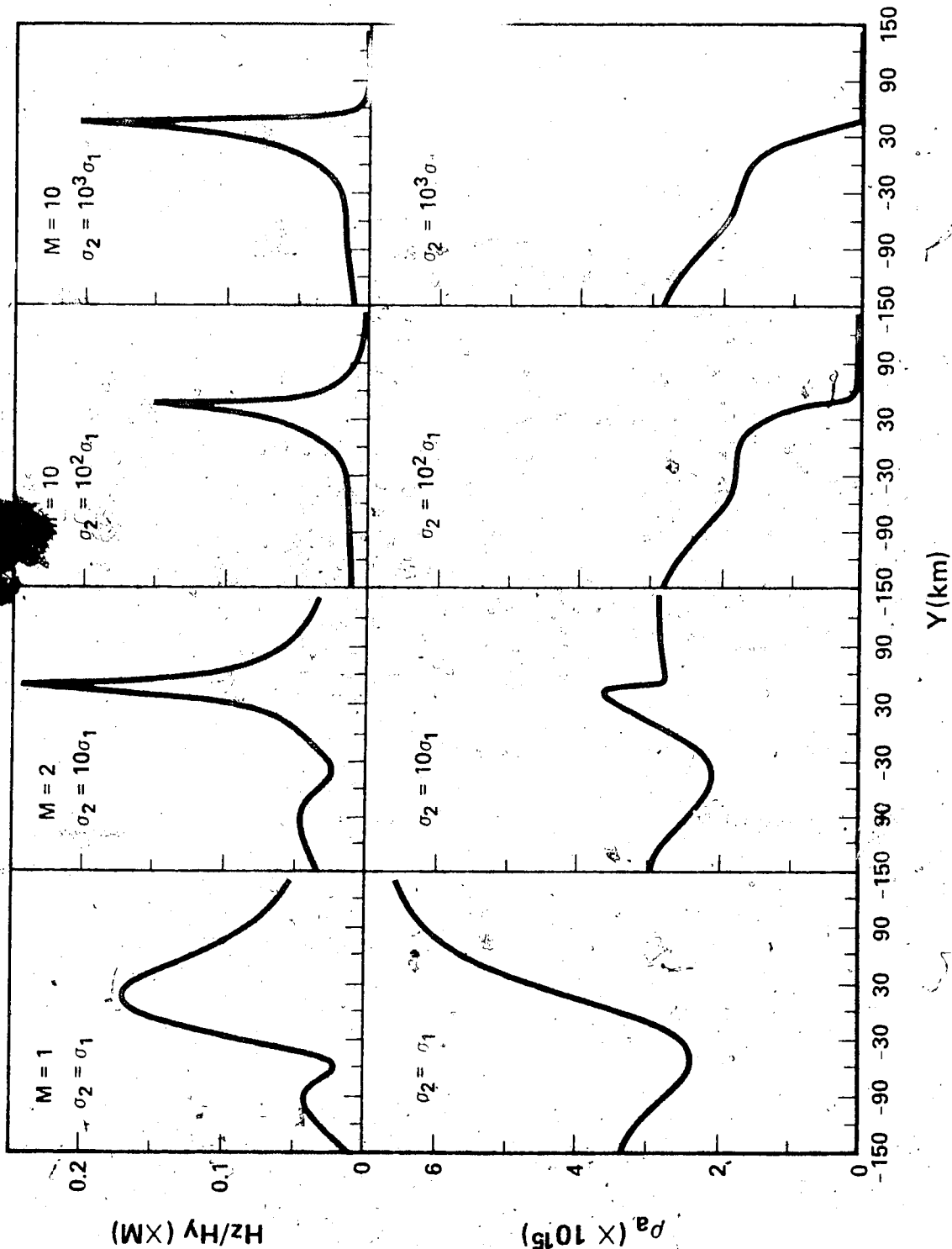


Fig. 26. The spatial variation of  $H_z/H_y$  and  $\rho_a$  at the surface  $z = -0$  for different upper layer conductivity contrasts for model D, with  $d = 2$  km and  $\sigma_1 = 10^{-15}$  emu. (The boundary between  $\sigma_1$  and  $\sigma_2$  is located at  $y = 47.5$  km.)

boundary between  $\sigma_1$  and  $\sigma_2$  is located at  $y = 47.5$  km. For convenience of display, different scale factors are used in the results for  $H_z/H_y$ . For example, taking into account the scale factors shown in Fig. 26, the maximum amplitudes of  $H_z/H_y$  should read as 0.17, 0.49, 1.5 and 2.0 for  $\sigma_2/\sigma_1 = 1, 10, 10^2$ , and  $10^3$  respectively. The behaviour of  $H_z/H_y$  for the model in which  $\sigma_2/\sigma_1 = 1$  is similar to that shown in Fig. 24 for model D. Since, in this case, the upper layer is uniformly conducting, the variation in the field components as a function of  $y$  can be interpreted as due to subsurface temperature variations only. The results indicate, that as  $\sigma_2$  increases, the effect of the upper layer conductivity contrast increases and the effect of temperature variations is dominated by the upper layer contrasts. This is evident from the sudden increase in the amplitude of  $H_z/H_y$  near  $y = 47.5$  km for large values of  $\sigma_2$ . Since  $\sigma_2/\sigma_1 = 10^3$  is of the same order as that for the sea-continent interface, the results for  $\sigma_2/\sigma_1 = 10^3$  would be applicable to the sea-land model in which  $\sigma_2$  represents the sea. Thus, from these results, it is apparent that large conductivity contrast at the surface dominates the behaviour of the magnetic field ratios and the apparent resistivity to the extent that the effect of the subsurface temperature variations is suppressed. Although the effect of the surface conductivity contrast will in general be different for different frequencies, its predominance in this model may be due to its location ( $y = 47.5$  km) which is not far from the region (near  $y = 35$  km) where the surface heat flow

undergoes a rapid variation.

#### 4.3 Summary of Results

The results presented in the previous section describe the behaviour of time-varying electromagnetic fields corresponding to heat flow distributions associated with a downgoing slab. From the results presented for a uniformly conducting upper layer several aspects of slab dynamics may be investigated. In the case of a descending slab heated only by conduction, the results indicate considerable variation in the vertical magnetic component ( $H_z$ ) as well as the magnetic field ratio  $H_z/H_y$ . The effect of the cold descending slab is to increase both of these quantities over the region of slab descent. The effect of shear heating along the upper surface of the slab causes a slight increase in the value of the horizontal magnetic component  $H_y$  with little effect on the other field components. The inclusion of rising melt from the upper surface of the slab causes significant variations in the electric and magnetic field components with the largest variations observed in the vertical magnetic component ( $H_z$ ) and the magnetic field ratio  $H_z/H_y$ .

From the above results the study of electric and magnetic fields in subduction zones may be used to study slab motion. A decrease in the apparent resistivity may be indicative of melted material rising from the top of the descending slab as well as corresponding increases in the

magnetic field components. The effect of a slab descending with no melting along the upper surface is to increase apparent resistivity while decreasing the horizontal magnetic component. When a lateral conductivity contrast is introduced in the upper layer, the results show that the effect of the temperature variation in the lower layer is reduced, and that, for a large conductivity contrast (e.g., sea-land interface), the subsurface temperature variation has little effect on the surface electromagnetic fields. Although this result is expected on the basis that currents induced in good conductors flow near the surface, in this model, the dominance of the surface conductivity contrast over the subsurface temperature variations is probably due to the closeness in the location where the heat flow varies rapidly. This aspect of the screening effect of the surface conductivity contrast as well as the effects on the electromagnetic fields of different frequencies requires further investigation.

## REFERENCES

- AKIMOTO, S. and H. FUJISAWA, Demonstration of the electrical conductivity jump produced by the olivine-spinel transition, *J. Geophys. Res.*, 70: 443-449, 1965.
- ANDREWS, D.J. and N.H. SLEEP, Numerical modelling of tectonic flow behind island arcs, *Geophys. J.R. Astr. Soc.*, 38: 237-251, 1974.
- ARONSON, J.R., L.H. BELLOTTI, S.W. ECKROND, A.G. EMSLIE, R.K. McCONNELL and P.C. VON THUNA, Infrared spectra and radioactive thermal conductivity of minerals at high temperature, *J. Geophys. Res.*, 75: 3443-3456, 1970.
- BENIOFF, H., Orogenesis and deep crustal structure: Additional evidence from seismology, *Bull. Geol. Soc. Amer.*, 65: 385-400, 1954.
- BIRD, P., M.N. TOKSOZ and N.H. SLEEP, Thermal and mechanical models of continent-continent convergence zones, *J. Geophys. Res.*, 80: 4405-4416, 1975.
- BREWITT-TAYLOR, C. R. and J.T. WEAVER, On the finite-difference solution of two-dimensional induction problems, *Geophys. J.R. Astr. Soc.*, 47: 375-396, 1976.
- DE BREMAECKER, J.C., Is the oceanic lithosphere elastic or viscous?, *J. Geophys. Res.*, 82: 2001-2004, 1977.
- DYRELIUS, D. and A. VOGEL, Improvement of convergency in iterative gravity interpretation, Report No. 5, Dept of Solid Earth Physics, University of Uppsala, 1971.
- GARLAND, G.D., Correlation between electrical conductivity and other geophysical parameters, *Phys. Earth and Planet. Interiors*, 10: 220-230, 1975.
- GOUGH, D.I., The geophysical significance of geomagnetic variation anomalies, *Phys. Earth and Planet. Interiors*, 1: 379-388, 1973.
- GRIGGS, D.T., The sinking lithosphere and the focal mechanism of deep earthquakes, from The Nature of the Solid Earth ed. by E.C. Robertson, J.P. Hays and L. Knopoff, 361-384, 1972.
- GROW, J.A. and C.O. BOWIN, Evidence for high-density crust and mantle beneath the Chile trench due to the descending lithosphere, *J. Geophys. Res.*, 80: 1449-1485, 1975.
- HANKS, T.C. and J.H. WHITCOMB, Comments on paper by John W.

- Minear and M. Nafi Toksoz, 'Thermal regime of a downgoing slab and new global tectonics', J. Geophys. Res., 76: 613-616, 1971.
- HASEBE, K.N. FUJII and S. UYEDA, Thermal processes under island arcs, Tectonophysics, 10: 335-355, 1970.
- HATHERTON, T. and W.R. DICKINSON, The relationship between andesitic volcanism and seismicity in Indonesia, the Lesser Antilles, and other island arcs, J. Geophys. Res., 74: 5301-5310, 1969.
- HAYES, D.E., A geophysical investigation of the Peru-Chile trench, Marine Geology, 4: 309-351, 1966.
- HORAI, K. and S. UYEDA, Terrestrial heat flow in volcanic areas, in The Earth's Crust and Upper Mantle, Geophys. Monograph 13, ed. by P.J. Hart, 95-109, American Geophysical Union, Washington, D.C., 1969.
- ISACKS, B., J. OLIVER and L.R. SYKES, Seismology and the new global tectonics, J. Geophys. Res., 73: 5855-5899, 1968.
- JONES, F.W., Induction in laterally non-uniform conductors: Theory and numerical models, Phys. Earth and Planet. Interiors, 7: 282-293, 1973.
- JONES, F.W. and L.J. PASCOE, A general computer program to determine the perturbation of alternating electric currents in a two-dimensional model of a region of uniform conductivity with an embedded inhomogeneity, Geophys. J.R. Astr. Soc., 24: 3-30, 1971.
- KATSUMATA, M. and L.R. SYKES, Seismicity and tectonics of the western Pacific, Izu-Mariana, Caroline and Ryukyu-Taiwan regions, J. Geophys. Res., 74: 5923-5948, 1969.
- KNODEL, K., A comprehensive investigation into the central European conductivity anomaly, Phys. Earth and Planet. Interiors, 1: 309-316, 1968.
- KUNO, H., Origin of andesite and its bearing on the island arc structure, Bull. Volcanol., 32: 141-176, 1968.
- LAW, L.K. and R.P. RIDDIHOUGH, A geographical relation between geomagnetic variation anomalies and tectonics, Can. J. Earth Sci., 8: 1094-1106, 1971.
- LEE, W.H.K. and S. UYEDA, Review of heat flow data, in Terrestrial Heat Flow, Geophys. Monograph 8, ed. by W.H.K. Lee, 87-190, American Geophysical Union, Washington, D.C., 1965.

- LE PICHON, X., J. FRANCHETEAU and J. BONNIN, Plate Tectonics, 300 pp., Elsevier, New York, 1973.
- LISTER, C.R.B., Tectonic movement in the Chile trench, *Science*, 173: 719-722, 1971.
- LLIBOUTRY, L., Sea-floor spreading, continental drift and lithosphere sinking with an asthenosphere at melting point, *J. Geophys. Res.*, 74: 6525-6540, 1969.
- LUDWIG, W.J., J.E. EWING, M. EWING, S. MURAUCHI, N. DEN, S. ASANO, H. HOTTA, M. HAYAKAWA, T. ASANUMA, K. ICHIKAWA, and I. NOGUCHI, Sediments and structure of the Japan trench, *J. Geophys. Res.*, 71: 2121-2137, 1966.
- MACDONALD, G.J.F., Calculations of the thermal history of the earth, *J. Geophys. Res.*, 64: 1967-2000, 1959.
- MALAHOFF, A., Some possible mechanisms for gravity and thrust faults under ocean trenches, *J. Geophys. Res.*, 75: 1992-2001, 1970.
- MCKENZIE, D.P., Speculations on the consequence and causes of plate motions, *Geophys. J. R. Astr. Soc.*, 18: 1-32, 1969.
- MCKENZIE, D.P. and J. SCLATER, Heat flow inside the island arcs of the Northwestern Pacific, *J. Geophys. Res.*, 73: 3178-3179, 1968.
- MERCIER, J.C. and N.L. CARTER, Pyroxene geotherms, *J. Geophys. Res.*, 80: 3349-3362, 1975.
- MINEAR, J.W. M.N. TOKSOZ, Thermal regime of a downgoing slab and new global tectonics, *J. Geophys. Res.*, 75: 1397-1419, 1970.
- MINEAR, J.W. and M.N. TOKSOZ, Reply, *J. Geophys. Res.*, 76 (2), 610-612, 1971.
- NIBLETT, E.R., K. WHITHAM and B. CANER, Electrical conductivity anomalies in the mantle and crust in Canada, The Application of Modern Physics to the Earth and Planetary Interiors, ed. by S.K. Runcorn, Wiley-Interscience, 1969.
- OXBURGH, E.R. and D.L. TURCOTTE, Problem of high heat flow and volcanism associated with zones of descending mantle convective flow, *Nature*, 216: 1041-1043, 1968.
- OXBURGH, E.R. and D.L. TURCOTTE, Thermal structure of island arcs, *Bull. Geol. Soc. America*, 81: 1665-1688, 1970.
- PASCOE, L.J. and F.W. JONES, Boundary conditions and



- calculation of surface values for the general two-dimensional electromagnetic induction problem, *Geophys. J.R. Astr. Soc.*, 27: 179-193, 1972.
- PEACEMAN, D.W. and H.H. RACHFORD, JR., The numerical solution of parabolic and elliptic differential equations, *J. Soc. Ind. Appl. Math.*, 3: 28-41, 1955.
- RICHTER, H.F., Dynamic models of sea floor spreading, *Rev. Geophys. and Space Physics*, 11: 223-287, 1973.
- RIKITAKE, T., Geophysical evidence of the olivine-spinel transition hypothesis in the earth's mantle, *Bull. Earthq. Res. Inst.*, 37: 423-431, 1959.
- RIKITAKE, T., Electromagnetism and the Earth's Interior, Elsevier, Amsterdam, 1966.
- RIKITAKE, T. and K. WHITHAM, Interpretation of the Alert anomaly in geomagnetic variations, *Can. J. Earth Sci.*, 1: 35-62, 1964.
- SCHMUCKER, U., Erdmagnetische Tiefensondierung in Deutschland 1957-1959: Magnetogramme und erste Auswertung. *Abhandl. Akad. Gottingen, Math. Physik. Kl., Beitr. I.G.J.*, 5: 1-51, 1959.
- SCHMUCKER, U. Anomalies of geomagnetic variations in the southwestern United States, *Bull. Scripps Inst. Oceanogr., Univ. California Press*, 1964.
- SCHÜBERT, G., C. FROIDEVAUX and D.A. YUEN, Oceanic lithosphere and asthenosphere: Thermal and mechanical structure, *J. Geophys. Res.*, 81: 3525-3540, 1976.
- SPENCE, W., The Aleutian arc: Tectonic blocks, episodic subduction, strain diffusion, and magma generation, *J. Geophys. Res.*, 82: 213-230, 1977.
- STAUDER, W., Mechanism of the Rat Island earthquake sequence of February 4, 1965, with relation to island arcs and sea floor spreading, *J. Geophys. Res.*, 73: 3847-3858, 1968a.
- STAUDER, W., Tensional character of earthquake foci beneath the Aleutian trench with relation to sea floor spreading, *J. Geophys. Res.*, 73: 7693-7701, 1968b.
- SUGIMURA, A. and S. UYEDA, Island Arcs: Japan and its Environs, Elsevier, Amsterdam, 1973.
- SYKES, L.R., The seismicity and deep structure of island arcs, *J. Geophys. Res.*, 71: 2981-3006, 1966.
- TOKSOZ, M.N., J.W. MINEAR and B.R. JULIAN, Temperature field

- and geophysical effects of a downgoing slab, J. Geophys. Res., 76: 1113-1138, 1971.
- TURCOTTE, D.L. and G. SCHUBERT, Frictional heating of the descending lithosphere, J. Geophys. Res., 78: 5876-5886, 1973.
- TURCOTTE, D.L. and E.R. OXBURGH, Mantle convection and the new global tectonics, Annu. Rev. Fluid Mech., 4: 33-68, 1972.
- UYEDA, S. and T. RIKITAKE, Electrical conductivity anomaly and terrestrial heat flow, J. Geomag. Geoelectr., 22: 75-90, 1970.
- VACQUIER, V., S. UYEDA, M. YASUI, J. SCLATER, C. CORRIE and T. WATANABE, Studies of the thermal state of the earth, 19th paper: heat flow measurements in the northern Pacific, Bull. Earthq. Res. Inst., 44: 1526-1554, 1966.
- VON HERZEN, R. P. and W.H.K. LEE, Heat flow in oceanic regions, in The Earth's Crust and Upper Mantle, Geophys. Monograph 13, ed. by P.J. Hart, 88-95, American Geophysical Union, Washington, D.C., 1969.
- WALCOTT, R.E., Flexure of the lithosphere at Hawaii, Tectonophysics, 9: 435-446, 1970.
- WARREN, R.E., J.G. SCLATER, V. VACQUIER and R.F. ROY, A comparison of terrestrial heat flow and transient geomagnetic fluctuations in the southwestern United States, Geophysics, 34: 463-478, 1969.
- WATTS, A.B. and M. TALWANI, Gravity anomalies seaward of deep-sea trenches and their tectonic implications, Geophys. J.R. Astr. Soc., 36: 57-90, 1974.
- WILLIAMSON, K., C. HEWLETT and H.Y. TAMMAMAGI, Computer modelling of electrical conductivity structures, Geophys. J.R. Astr. Soc., 37: 533-536, 1974.
- YODER, H.S. and C.E. TILLEY, Origin of basalt magmas: An experimental study of natural and synthetic rock systems, J. Petrol., 3: 342-532, 1962.